

**Ministry of Education and Science of Russian Federation
Moscow Institute of Physics and Technology)**

Applied physics and research department
Russian Quantum Center
Quantum computation with cold calcium ions

BACHELOR DIPLOMA

Ion dynamics in Surface Electrode Traps

Author:
Artem Sergeevich Podlesnyy

Scientific supervisor:
Dr. Kirill Eugenievich Lakhmanskiy

Mentor:
Yelnury Suleimen



Moscow 2022

Abstract

Ion dynamics in Surface Electrode Traps

Podlesnyy Artem Sergeevich

Quantum computers are expected to exponentially decrease the solution time on the number of tasks, possessing a high significance, such as optimization, prime factorization and database search. Possible applications also include quantum chemistry (drug discovery and new materials), quantum machine learning. Quantum technologies are rapidly developing over the past decades, with several platforms already achieving quantum supremacy. However, to have practical value, quantum computers are to increase their number of logical qubits by an order of magnitude.

Among the main platforms for this task is the trapped-ion quantum computer, with the highest reported coherence time and fidelity of one- and two-qubit operations. One of the most promising approaches for scaling ion-based system lies in using surface electrode traps (SET). Microchip technologies allow the manufacture of complicated arrays of the electrodes, ensuring precise and flexible control of ions above the surface, also giving plenty of space for control and readout. For the successful ion trapping and control, it is necessary to perform simulations of the potential, ion motion, to obtain parameters, describing the system, prior to fabrication and experiment. For this purpose, two Python packages are presented in the diploma. The first package simulates potential distribution above the arbitrary surface trap, while the second package performs a highly accurate modeling of ion motion above the SET. The results of the work capture important details, for example – stability of motion of several ions, which is an unsolved theoretical task. My work is already used for determining design of the SETs, being fabricated by the group, and will be useful for the trap analysis in future.

Contents

1	Introduction	5
2	Quantum Computation with Trapped-Ions	9
2.1	Ion Trapping	9
2.1.1	Linear Paul trap	9
2.1.2	Surface traps	11
2.2	Ion Qubit	12
2.2.1	Laser-Ion Interaction	12
2.2.2	Cooling	14
2.2.3	Control and readout	16
2.3	Ion motion in the trap	17
2.3.1	Coulomb crystals	17
2.3.2	Normal modes	19
2.3.3	Quantization and coupling	20
3	Simulation of Surface Traps	23
3.1	Analytic model of a surface trap	23
3.1.1	Ion motion near potential minima	23
3.1.2	Potential distribution above the surface	25
3.1.3	Gapless approximation	27
3.1.4	Cover plate influence	27
3.1.5	Micromotion compensation	28
3.1.6	Stability analysis	29
3.2	Python simulation of SET	31
3.2.1	Program description	31
3.2.2	Verification	34
3.2.3	Technical requirements	35
4	Ion dynamics simulation in Surface Trap	37
4.1	Python modeling of ion motion	37
4.1.1	Molecular Dynamics Method	37
4.1.2	Surface trap case	39
4.2	SID package	40
4.2.1	Program description	41
4.2.2	Technical requirements	43
4.3	Phase transitions in Coulomb crystals	44
4.4	Verification	46
4.4.1	Ion crystal	46
4.4.2	Transition law	47
4.4.3	Normal modes verification	49
4.5	Result: trap design for five ions	50

5 Conclusion	53
5.1 Summary	53
5.2 Comparison with existing results	53
5.2.1 SET simulation	53
5.2.2 Ion dynamics simulation	53
5.3 Outlook	54

Chapter 1

Introduction

Quantum computing has been an uprising topic for the past two decades. The idea behind it lies in using the laws of quantum physics to create quantum bits of information, and perform computations with them. Two main components are quantum bits - qubits, and entanglement. Unlike classical information bits, which take only two possible values - 0 and 1, qubits are in the superposition of these states:

$$|\psi\rangle = \alpha|0\rangle + \beta|1\rangle, \alpha^2 + \beta^2 = 1. \quad (1.1)$$

That means qubits have much broader state space, which can be used to encode information. To consider several qubits, in quantum information theory the qubit registers are introduced:

$$|\psi_{\text{register}}\rangle = \alpha_0|00..00\rangle + \alpha_1|00..01\rangle + \dots + \alpha_{2^n-1}|11..11\rangle, \quad (1.2)$$

where n is the qubit number.

The quantum entanglement definition is a more complicated topic. Consider the Bell state $1/\sqrt{2}(|00\rangle + |11\rangle)$, which is called a fully entangled state. Using Dirac's notation and von Neumann postulate, let's find the resulting state after measurement (in the computational basis) of the first qubit in the state $|0\rangle$:

$$|\psi_{\text{result}}\rangle = \frac{1}{\sqrt{2 \times Pr(|0\rangle)}} \langle 0| (|00\rangle + |11\rangle) = |0\rangle, \quad (1.3)$$

where $Pr(|0\rangle)$ is the probability of measurement outcome 0. This result shows us that if we measure one of the entangled qubits and obtain the result, we will immediately know the state of the second qubit. This particular example leads to a well-known quantum teleportation algorithm^[1]. This ability to influence the whole system by operating with only its part is known as quantum entanglement.

There are also other properties of quantum systems that can be used to improve classical algorithms, such as quantum tunneling (quantum annealing)^[2], adiabatic theorem (adiabatic quantum computing)^[3], quantum measurement (one-way quantum computing)^[4] and other techniques. These properties form different branches of quantum computing, such as mentioned above, but are out of scope of this diploma.

Using these features it is possible to construct algorithms, significantly outperforming classical analogs in some particular tasks. The class of such problems is generally referred to as BPQ – bounded-error quantum polynomial time^[5], and stands for the problems (from P and NP classes), which can be solved by the quantum computer in polynomial time. One of the most famous examples is the Shor's algorithm of prime number factorization^[6].

Current most widely-used cryptosystem, RSA, which encrypts keys as a product of two large prime numbers, relies on the fact that the reverse process is impossible to perform on today's classical computers. However, with an ideal (and sufficiently big) quantum computer it is possible to perform such factorization in polynomial time, thus breaking this protocol. That's one of the key factors of the growing interest towards quantum computers.

Another important direction of the research is application of quantum computing to optimization problems^[7]. This implies constraint and unconstrained combinatorial optimization, quantum chemistry and quantum machine learning. In these tasks it is possible to achieve quantum advantage in the nearest future. These advantages are highly economically impactful due to their various applications in practical tasks (such as Traveling Salesman Problem, or drug discovery).

However, quantum computers must go a long way to achieve the described advantage. They are now in the phase, called the NISQ-era. Noisy Intermediate-Scale devices consist of 100-1000 physical qubits with only finite precision. That means that we are limited in the number of algorithms we can use on today's devices, and their results do not outperform classical computers. With that, the main focus of modern research is in creating a fault-tolerant quantum computer – a large-scale computer with efficient error-correction codes.

The qubits used in NISQ devices are called physical qubits – an implementation of a controlled quantum two-level system. The general approach to perform error-correcting in quantum computing is to operate with a number of physical qubits to encode one logical qubit, which is robust towards errors. The number of the required physical qubits is strongly dependent on the fidelity of two-qubit quantum gates – computational operations on two qubits, performing their entanglement^[8]. This fact is represented on figure 1.1.

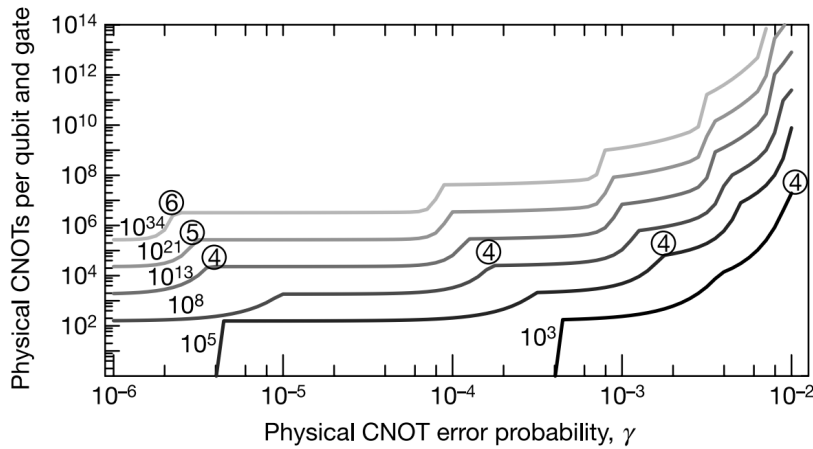


Figure 1.1: A dependence of the number of physical CNOT operations, required to perform a logical CNOT operation, on the infidelity of the physical CNOT gate. $N_{CNOT} \propto N_{physical}$ – a number of physical qubits, encoding a logical qubit. The plots represent the dependence for several computational sizes G – a number of such operations in the algorithm.

One of the most promising physical platforms is trapped-ion quantum computing^[9]. Here, the qubits are electronic states of an ion, confined in the RF or Penning trap. Compared to other quantum computing platforms, the trapped-ion quantum computing demonstrates the highest fidelity of one and two-qubit operations^[10], which is important

not only for NISQ-era, but allows to decrease a number of physical qubits, necessary for fault-tolerant computing. Also, the coherence time of ion qubit is the highest, reaching 1 hour. This is a time period, in which the quantum system is robust towards decoherence – a process of accumulation of errors.

These two achievements allow ion computers to fulfill all of the DiVincenzo criteria [11] for an efficient quantum computer, except one – the scalability of the system. Highest number of ion qubits today demonstrate a Honeywell computer – 20^[12]. And the process of scaling is extremely challenging, due to the number of factors.

One of the most promising approaches lies in using Surface Electrode Traps^[13], which is a set of electrodes, placed on the 2D plane, confining charged particles above the chip. The use of surface, or planar traps over conventional Paul or Penning traps is motivated by several factors. An ability to place an arbitrary number of electrodes increases the degrees of freedom of the system, allowing to obtain a flexible control of ions. And because all the electrodes are placed on the surface, this gives a wide room for an optical setup to be implemented in the most optimal manner. Another advantage of the surface geometry is an ability to implement all the necessary detectors, optical lasers and voltage sources^[14] on the chip's surface, thus decreasing the size of the computer.

One of the most researched proposals is based on shuttling short ion crystals^[15], which is only possible to implement with surface traps. This shuttling, however, requires a too long time for practical calculations, which is one of the leading research focuses of today's ion computing.

These facts describe an interest towards surface traps for quantum computing applications. In the research group "Quantum Computation with cold Ca+ ions" of the Russian Quantum Center, we are developing a first Russian quantum computer on SET technology. And the first step to design the planar trap is to be able to simulate it. In this diploma I describe two Python packages, which we developed for simulating ion dynamics above the SET.

Chapter 2

Quantum Computation with Trapped-Ions

All simulations in this diploma were carried for the $^{40}\text{Ca}^+$ ions trapped in surface radio-frequency (RF) linear traps. In this chapter the theoretical background of quantum computing with trapped ions is given. In section 2.1 the basics of trapping in RF traps are described. The section 2.2 provides the description of ion qubits and their operations. In section 2.3 the ion motion is described from the classical point of view. Lastly, section 2.4 deals with the heating in RF traps, which is a huge problem for surface traps.

2.1 Ion Trapping

Before anything, we need to trap ions in a stable way. Due to the ion nature being a charged particle, the main idea is to use electric or/and magnetic fields to trap them in free space. However, according to Earnshaw's theorem it is not possible to confine a charged particle in the electrostatics field alone.

This problem was solved by Wolfgang Paul by inventing the radio-frequency ion trap (Nobel Prize 1989). Here, the charged particle is confined in the combination of the static (DC) and oscillating (RF) electric fields^[16].

2.1.1 Linear Paul trap

The typical Paul trap consists of four symmetric, hyperbolically shaped RF electrodes, encircling a potential tube, and two opposite hyperbolical electrodes on the two ends of the trap, called endcaps (figure 2.1)^[17]. The endcaps are used to confine the ions axially (in the direction of the tube's axis). Consider the four symmetric electrodes.

If the voltages $\pm \frac{V_{RF}}{2} \cos(\Omega_{RF}t)$ are applied on the electrodes, such that the electrodes with the same sign are opposite, the total quadrupole potential will be

$$\Phi(x,y,t) = \frac{V_{RF}}{2d^2}(x^2 - y^2) \cos(\Omega_{RF}t), \quad (2.1)$$

where $2d$ is the separation of two opposite electrodes. With that potential, equations of motion are

$$\ddot{x} = -\frac{V_{RF}Q}{d^2m}x \cos(\Omega_{RF}t), \quad (2.2)$$

$$\ddot{y} = \frac{V_{RF}Q}{d^2m}y \cos(\Omega_{RF}t), \quad (2.3)$$

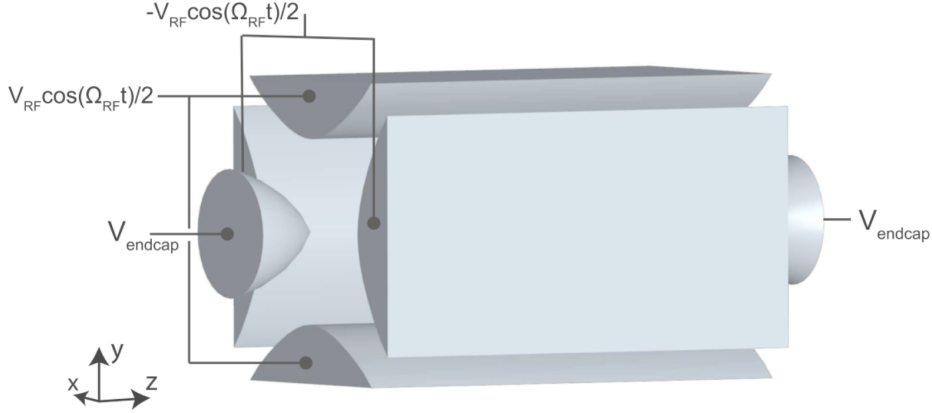


Figure 2.1: A standard linear Paul trap. An oscillating RF-voltage is applied on the four hyperbolic-shaped electrodes, inducing a pseudopotential distribution in the tube, which confines ion radially. Additional DC-voltages, called endcaps, confine ion axially. Figure courtesy of [17].

for an ion with mass m and charge Q . These are the simplest Mathieu equations. Their stability is well researched, and if we introduce a so called stability parameter:

$$q = \frac{2QV_{RF}}{md^2\Omega_{RF}^2}, \quad (2.4)$$

the stability of the trap will be in the region $0 < q < 0.908$ (assuming axial confinement). For more detailed consideration see section 3.1.6.

In the stability region, the ion motion can be expressed as a superposition of two modes of oscillation in the x-y plane. The first mode is called a micromotion. Its frequency is Ω_{RF} , and the amplitude is increasing with the distance of ion towards the RF potential minimum. This mode changes the linewidth of the transitions due to the Doppler broadening, which lowers the laser cooling efficiency, therefore it needs to be compensated (see section 3.1.5). With micromotion compensation, we can focus on the second motional mode.

The second mode is called secular motion, and has a smaller frequency (by the factor $q/\sqrt{8}$), and larger amplitude. That means, in the RF minimum we can move to the secular approximation, where the trapping potential is defined as a pseudopotential:

$$U_{\text{pseudo}} = \frac{1}{2}m\omega_{\text{sec}}^2(x^2 + y^2), \quad (2.5)$$

where

$$\omega_{\text{sec}} = \frac{QV_{RF}}{\sqrt{2}md^2\Omega_{RF}}. \quad (2.6)$$

Then, the ion motion can be interpreted as the motion in the trapping harmonic pseudopotential. The ω_{sec} of the oscillations, with x or y direction is called radial frequency ω_{rad} .

If we consider endcap DC electrodes now, their potential is

$$U(x,y,z) \approx \frac{1}{4}m\omega_z^2(2z^2 - x^2 - y^2), \quad (2.7)$$

with the axial frequency ω_z . This means axial confinement produces anti trapping potential in the radial plane, so they always have to be considered simultaneously.

2.1.2 Surface traps

Because of the form of the electrodes, the conventional Paul trap provides only limited access to the lasers, which is necessary for quantum logic. Additionally, as it will be shown in section 3.1.2, the micromotion compensation depends on the number of electrodes in the trap (as a degree of freedom). Although the wider optical access can be achieved in 3D Paul trap by using blade-shaped electrodes^[18], and additional electrodes can be used in the system for compensation, the process of 3D trap manufacture is very complicated and costly. It may be favorable to use Surface Electrode Traps (SETs) for ion trapping. The fabrication of surface traps is much easier, and a complicated electrode set is aligned on the production step, unlike the 3D traps, where this process introduces additional bias.

The simplest planar trap is pictured on figure 2.2. Here the idea can be understood – the hyperbolic 3D electrodes are mapped on the rectangular surface electrodes. The two RF electrodes, which are separated from each other by a central ground, induce the pseudopotential tube, trapping ions radially. And side DC electrodes are used, to induce the axial confinement.

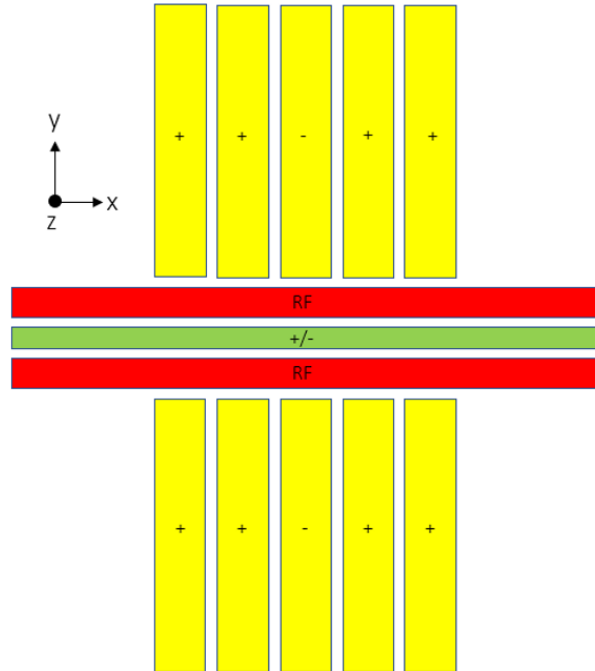


Figure 2.2: A five-wire trap design – the simplest design of the planar trap. Here two RF electrodes (depicted red) form a pseudopotential tube, trapping ions radially. Side DC electrodes (depicted yellow) form a potential well in axial direction. The central DC electrode (green) is used for compensation. Gaps between the electrodes are necessary for them to keep different voltages. In more precise calculation the capacity of these gaps should be taken into account.

In contrast to conventional Paul traps, SET doesn't provide a quadrupole potential in the whole trap. However, near the potential minimum, the potential can be considered as harmonical in the first expansion. The analytic model of the potential distribution is provided in section 3.1.2.

2.2 Ion Qubit

To implement the two-level system on a physical ion, the central part are laser-ion interactions. Ion cooling is achieved by laser cooling (doppler and sideband, 2.2.2). While qubit is encoded as the quantum states of the electron in the atom term, the most efficient way to control the states is through optical interactions. Furthermore it's required for atomic spectroscopy, which all is described in this section.

2.2.1 Laser-Ion Interaction

Consider two level approximation of the ion system, with $|g\rangle$ – ground state and $|e\rangle$ – excited state. Hamiltonian in the dipole approximation of the two levels of ion is represented as

$$\hat{H} = \hat{H}_t + \hat{H}_m + \hat{H}_i, \quad (2.8)$$

where \hat{H}_t is a Hamiltonian of two discrete energy levels:

$$\hat{H}_t = \frac{\hbar}{2}\omega_t\sigma_z, \quad (2.9)$$

where σ_z is a z-Pauli matrix, ω_t is a transition frequency.

The motional Hamiltonian \hat{H}_m in a harmonic potential is

$$\hat{H}_m = \hbar\omega_{x,y,z} \left(\hat{a}^\dagger \hat{a} + \frac{1}{2} \right), \quad (2.10)$$

where the creation \hat{a}^\dagger and annihilation operators \hat{a} describe respective motional modes $\omega = \omega_{x,y,z}$. Then energy eigenvalues $E_n = \hbar\omega(n + 1/2)$ with n being a phonon number.

The Hamiltonian of the interaction of laser beam with ion:

$$\hat{H}_i = \hbar\Omega(\sigma_+ + \sigma_-) \cos(k\hat{x} - \omega_l t), \quad (2.11)$$

where the laser field has frequency ω_l and the wave number k , $\sigma_\pm = \sigma_x \pm i\sigma_y$. Ω is a Rabi frequency, describing the interaction force between the ion and the laser field.

Let's now move to the interaction picture, by applying with $\hat{H}_0 = \hat{H}_t + \hat{H}_m$ the evolution operator $\hat{U} = e^{-i\hat{H}_0/\hbar}$ as $\hat{H}_I = \hat{U}^\dagger \hat{H}_i \hat{U}$:

$$\hat{H}_I = \frac{1}{2}\hbar\Omega \left(\sigma_+ e^{i\eta(\tilde{a} + \tilde{a}^\dagger)} e^{-i\Delta t} + H.c. \right). \quad (2.12)$$

Here $\tilde{a} = ae^{-i\omega t}$, and

$$\eta = kx_0 = k\sqrt{\frac{\hbar}{2m\omega}} \quad (2.13)$$

is the Lamb-Dicke parameter, indicating the relation of the width of wave packets of an ion in the ground state and the laser beam. The equation 2.12 was obtained with rotating wave approximation (RWA) – the neglection of the highest oscillations, and the Lamb-Dicke approximation: $\eta^2(2\bar{n} + 1) \ll 1$, where \bar{n} is the mean phonon number. This means that the wavelength of the laser is much bigger, than the width of the wave packet, describing ion motion. The so-called Lamb-Dicke regime is necessary for ion quantum computing.

The laser detuning $\Delta = \omega_l - \omega_t$ define several special cases for the Hamiltonian (see figure 2.3). If $|n\rangle$ is a motional state with n phonon number, than the equation 2.12 states, that two states with different motional modes can be coupled as $|g, n\rangle \leftrightarrow |e, m\rangle$. Thus, by detuning $\Delta \approx (m - n)\omega$ we can couple these modes.

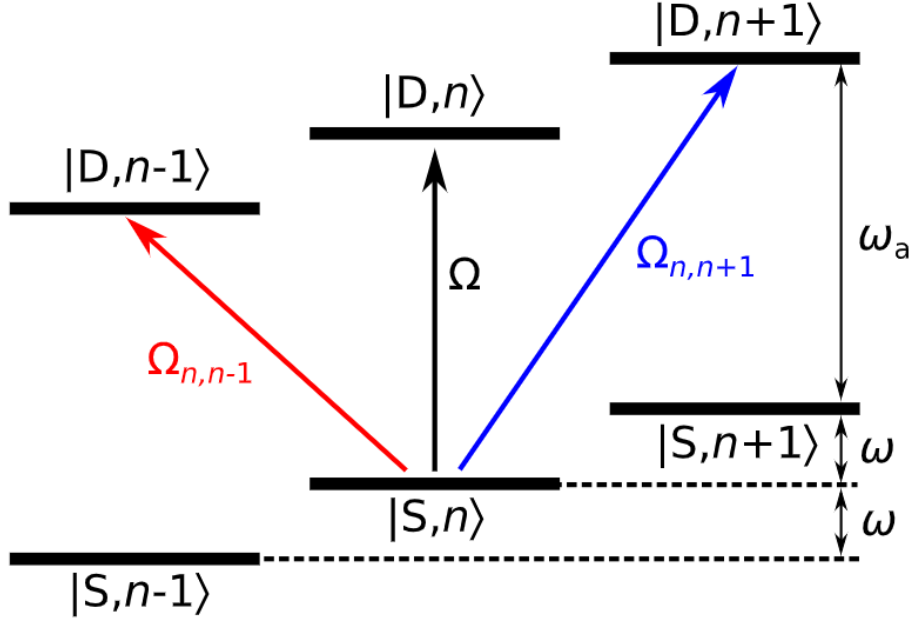


Figure 2.3: Energy level scheme of a quantum two-level system in harmonic trapping potential. The three special transitions, driven by laser light are shown. The **red** sideband transition decreases the phonon number, while the **blue** sideband increases. The carrier transition doesn't change the phonon number. Figure courtesy of [19].

The coupling strength between two modes is described by the Rabi frequency as

$$\Omega_{n,m} = \Omega_{m,n} = \Omega \left| \langle n | e^{i\eta(\hat{a} + \hat{a}^\dagger)} | m \rangle \right|. \quad (2.14)$$

In the Lamb-Dicke regime it can be simplified further for several special cases, discussed below.

Carrier transition. For $\Delta = 0$ the Hamiltonian becomes

$$H_C = \hbar \frac{\Omega_C}{2} (\sigma_+ + \sigma_-). \quad (2.15)$$

Then, the time evolution of the ion will be:

$$|\psi(t,n)\rangle = \cos \frac{\Omega t}{2} |g\rangle - i \sin \frac{\Omega t}{2} |e\rangle. \quad (2.16)$$

This means, that carrier transition doesn't affect motional modes, and it's Rabi frequency:

$$\Omega_C = \Omega_{n,n} = \Omega(1 - \eta^2 n). \quad (2.17)$$

Red sideband transition. For $\Delta = -\omega$ the Hamiltonian is

$$\hat{H}_{\text{red}} = i\hbar\eta \frac{\Omega}{2} (\sigma_+ \hat{a} - \sigma_- \hat{a}). \quad (2.18)$$

This Hamiltonian describes a transition $|g,n\rangle \rightarrow |e, n-1\rangle$, with a decrease in the phonon number, crucial for cooling, described in the section 2.2.2. The evolution of the state then

$$|\psi(t,n)\rangle = \cos \frac{\Omega_{\text{red}} t}{2} |g, n\rangle + \sin \frac{\Omega_{\text{red}} t}{2} |e, n-1\rangle, \quad (2.19)$$

with coupling strength

$$\Omega_{\text{red}} = \Omega_{n,n-1} = \eta\Omega\sqrt{n}. \quad (2.20)$$

Then, the probability of measuring the excited state with reduced phonon number is:

$$Pr(t,n) = \sin^2\left(\frac{\Omega_{\text{red}}t}{2}\right). \quad (2.21)$$

Blue sideband transition. For the $\Delta = \omega$, the Hamiltonian is:

$$\hat{H}_{\text{blue}} = i\hbar\eta\frac{\Omega}{2}(\sigma_+\hat{a} - \sigma_-\hat{a}). \quad (2.22)$$

For the coupling strength

$$\Omega_{\text{blue}} = \Omega_{n,n+1} = \eta\Omega\sqrt{n+1}, \quad (2.23)$$

the evolution of the system is

$$|\psi(t,n)\rangle = \cos\frac{\Omega_{\text{blue}}t}{2}|g,n\rangle + \sin\frac{\Omega_{\text{blue}}t}{2}|e,n+1\rangle. \quad (2.24)$$

So the blue sideband describes the transition to the state with increased phonon number – heating.

2.2.2 Cooling

The temperature of a single particle is measured as a mean phonon number of its motion, describing its kinetic energy. In order to perform high fidelity operations, the ions in the trap have to be cooled to the ground motional state. In practice it is unattainable, however with the phonon number close enough to the ground state, the high fidelity can be achieved. Typically the operational temperature of the ions in trap can reach 0.1^[20] phonons. In this section the general procedure for ion cooling is reported, although there are several state-of-the art cooling techniques being developed, for example EIT cooling^[21].

The ground state temperatures are usually achieved by applying two consecutive laser cooling techniques. First, the ions are cooled down by Doppler cooling to the Doppler limit, which occurs in the Lamb-Dicke regime. Then, ions achieve ground state by the sideband cooling.

Doppler cooling

The Doppler cooling can be understood by the semi-classical approach. The natural linewidth of the transition for Doppler cooling $\Gamma \gg \omega$ which is called weak-binding regime. Consider a two-leveled system (ion) in the laser field (figure 2.4).

Due to the Doppler effect, depending on the velocity of the ion, the laser frequency will be shifted in the frame of reference of the ion. Consider the laser beam with the detuning Δ from the ion's resonance. That means, that if the Doppler shift doesn't compensate detuning, the photon will be scattered on the ion, but for the some critical velocity, the photon will be absorbed by the two-leveled system, and it's momentum will be changed by the momentum of the photon. In particular, while an ion moves towards the laser beam with red detuning, the ions with the higher speed will absorb the photon, and reduce their momentum, while the ions with lower speed won't.

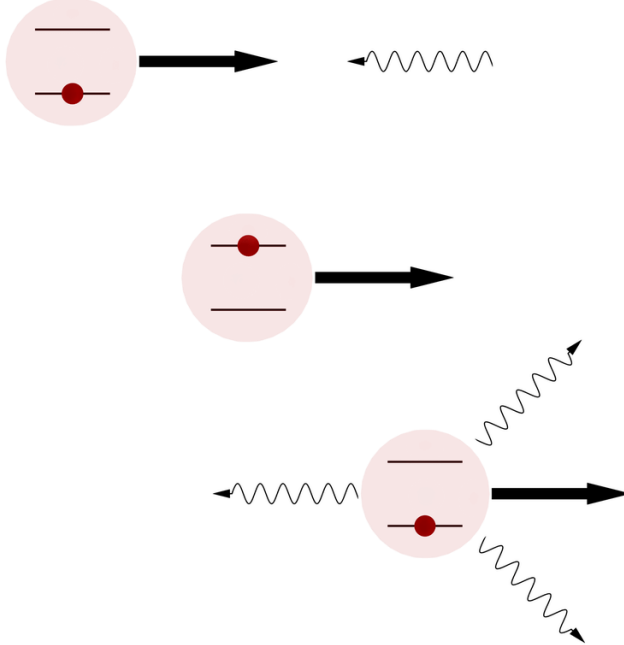


Figure 2.4: A sequence of Doppler cooling process. The ion in ground states absorbs the red-detuned light, depending on the velocity direction, popping to the excited state with reduced momentum. Then the decay occurs in the random direction, which randomly changes the ion's momentum. Figure courtesy of [22].

Ions in the harmonic trap are periodically oscillating. And applying a laser beam with red detuning will lead to a cooling process. For the cooling of all motional modes, there need to be at least three laser beams to couple with all motional modes. However, for an ion in the harmonic trap, its motion is decomposed to three perpendicular motional modes, and a single laser beam, which will be coupled to all three modes due to a laser's direction, is enough for efficient cooling.

However, the produced excited state decays to the ground state with the photon emission in random direction, thus obtaining a random momentum. The combination of these two processes cool down ions, but due to this random walk in momentum space, the cooling is limited by the minimum energy (Doppler limit):

$$E_D = \frac{\hbar\Gamma}{2}. \quad (2.25)$$

The corresponding minimum mean phonon number of the trapped ion, achieved by detuning $\Delta = -\Gamma/2$:

$$n_{\min} \approx \frac{\Gamma}{2\omega}. \quad (2.26)$$

Typical Doppler limit is $n \sim 11^{[19]}$, and with a typical Lamb-Dicke parameter $\eta \sim 0.07$ the Lamb-Dicke regime can be reached.

Sideband cooling

The following cooling is achieved by sideband cooling. The process is depicted on figure 2.5. For cooling the ion a red sideband transition is used. The corresponding quadrupole transition in ${}^+{\text{Ca}}^{40}$ ions is $S_{1/2}-D_{5/2}$ with 729 nm laser.

However, the lifetime of the metastable D state is $\sim 1\text{s}$, so to obtain a sufficient cooling rate, the state is coupled to the short living state $P_{3/2}$ with a 854 nm laser. Thus

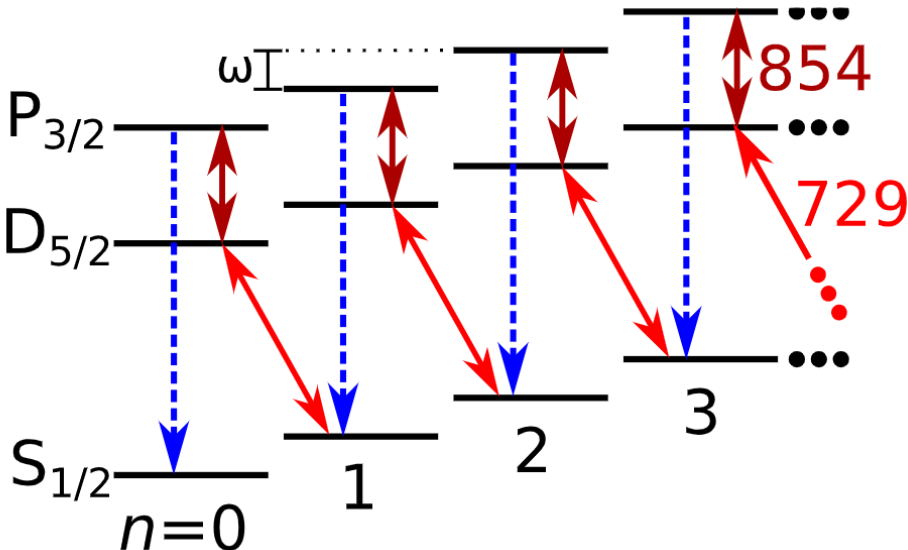


Figure 2.5: Sideband cooling scheme for $^{40}\text{Ca}^+$ ion. In every cycle by applying 729 nm laser a red sideband transition is induced with losing one phonon number, and the simultaneous 854 nm pumping transfers the state to a $P_{3/2}$ level. Then the qubit spontaneously decay to back to ground state $S_{1/2}$ with lesser phonon number. Figure courtesy of [19].

the excited state with reduced phonon number is quickly decaying to the ground state, and the cycle continues. Achieving the $|n = 0\rangle$ state the coupling strength to the red sideband becomes zero, and the ion remains in the ground motional state.

2.2.3 Control and readout

There are several criteria on how to choose the ion for a qubit implementation. Its energy levels are to be simple, for an efficient two-level approximation. And the transitions should be operable between levels. $^{40}\text{Ca}^+$ ion is a good choice, because while single, it has only one valence electron with a hydrogen-like energy spectrum. And all relevant transitions occur in the 390-870 nm range, which is accessible with modern lasers.

On the figure 2.6 the energy levels of $^{40}\text{Ca}^+$ are shown. To encode a qubit, the $|S\rangle$ and $|D\rangle$ states are used. While ignoring the Zeeman splitting, the S state is a $4^2\text{S}_{1/2}$ term, and D – $3^2\text{D}_{5/2}$ term. The D states have long life time ~ 1 s, and thus are called metastable states. The S-D transition is dipole forbidden, and is a quadrupole allowed transition. It is induced by applying a strong 729 nm laser beam.

The next higher energy terms $4^2\text{P}_{1/2}$ and $4^2\text{P}_{3/2}$ are short-lifetime states (~ 7 ns), and are dipole transitions for 4S and 3D states. The $4^2\text{S}_{1/2}$ - $4^2\text{P}_{1/2}$ transition is driven by a 397 nm laser and is used for Doppler cooling and state detection. However, there is the 7.5% possibility of decay to $D_{3/2}$, so the additional 866 nm pumping is used to suppress this decay into the D state.

And for the qubit encoding the 854 nm laser drives the $3^2\text{D}_{5/2}$ - $4^2\text{P}_{1/2}$ transition from metastable to a fast-decaying state. Considering Zeeman splitting, the transitions are shifted by 1.68 megahertz per Gauss (MHz/G) and 2.80 MHz/G for S and D levels respectively. For the operational transitions the Zeeman sublevels are chosen according to the robustness of the respective transition to the magnetic field fluctuations.

The state detection is usually performed with detection of photon emission due to the P-S decay. If the qubit state is $|S\rangle$, the 397 nm laser drives S-P transition, which due

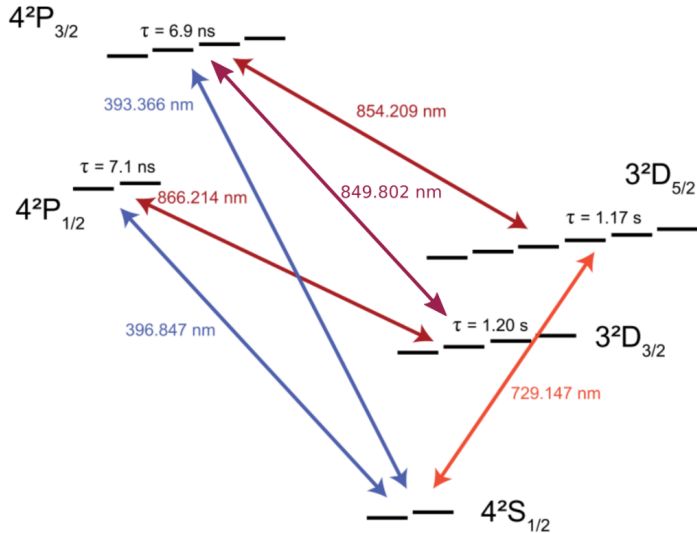


Figure 2.6: Energy levels of $^{40}\text{Ca}^+$ with transition frequencies between sublevels. The energy terms are splitted to Zeeman sublevels by the magnetic field of several Gauss. The relevant transitions between sublevels are chosen for their robustness to magnetic field fluctuation. Figure courtesy of [17].

to the short lifetime of the P state, rapidly decays with a photon emission. This process is repeated, and the detector receives millions of photons, which allows it to obtain a bright signal in ~ 1 ms. But the $|D\rangle$ state will be dark. This technique of optical mapping allows state detection with nearly 100% efficiency.

There are several detection techniques for the state measurement. It is sufficient to use a photomultiplier tube and a CCD camera for photon detection. However, surface traps allow the use of a superconducting nanowire single-photon detector (SNSPD)^[23] for measuring single photons. This way the speed of measurement is significantly increased.

2.3 Ion motion in the trap

Single qubit motion is relatively easy and is described by the equations above. However, with the increase in ion number, the complexity of calculating highly increases, and the many-ion dynamics can be only evaluated by the computer. For the implementation of quantum computing, however, it is necessary to do such computations. The gate implementation in ion-based quantum computing is based on their mechanical motion as a source of coupling between. And the long-range character of the Coulomb interaction allows the all-to-all connectivity between ions in the trap.

2.3.1 Coulomb crystals

The ions in the Paul traps are cooled to the ground state for quantum computing application. With such a small kinetic energy, the ion's motion can be represented as^[24]

$$x_m(t) \approx x_m^{(0)} + q_m(t), \quad (2.27)$$

the sum of equilibrium ion position $x_m^{(0)}$ and its small perturbation $q_m(t)$. This condensation of ions to their equilibrium positions is called Coulomb crystals (or Coulomb

crystallization), due to the similarities of the behavior to the conventional crystals. This structure is a building block of a trapped-ion quantum computing.

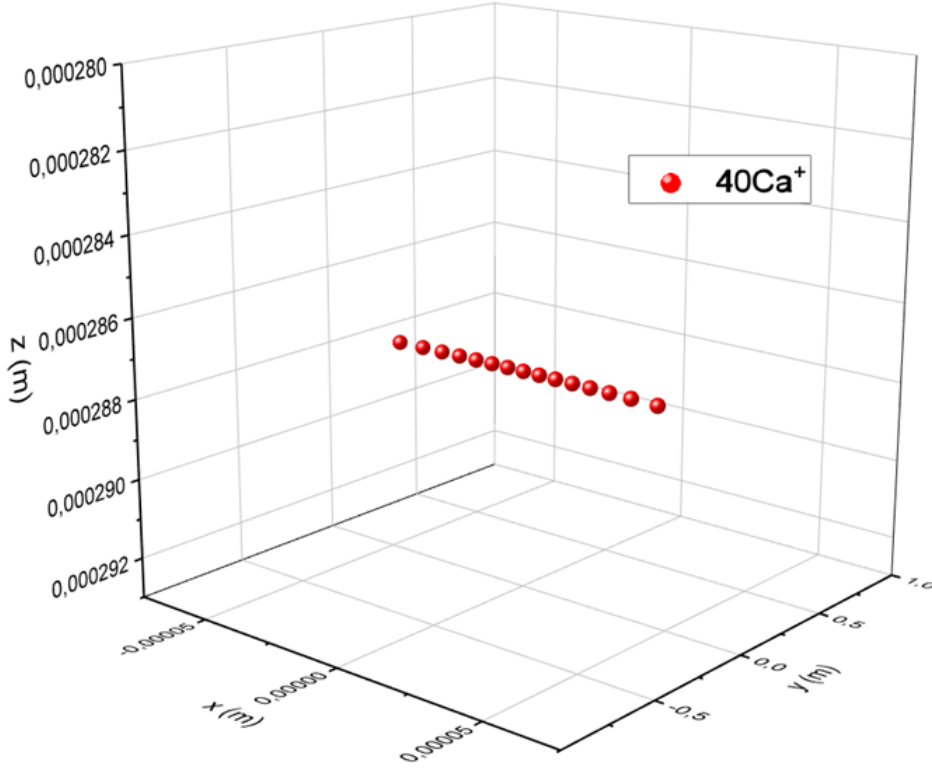


Figure 2.7: A Coulomb crystal, condensed in the SET as a linear ion chain, the most common type of ion crystals, used in trapped-ion quantum computing. The picture was obtained with the developed SID package (see chapter 4).

Usually, for quantum computing applications a linear ion chain is used (figure 2.7). The chain is distributed along the axial axis of the trap. Such linear structures are the simplest and most developed objects for quantum gates realization, thus are the most popular. There are, however, other phases of Coulomb crystals to be researched (see section 4.3 for more details).

Let's consider a 1D chain in the axial potential with ω_{ax} frequency of N identical ions, with masses M and charges Ze . The potential (in harmonic approximation) is given by the trap potential, and Coulomb interaction between ions:

$$V = \sum_{m=1}^N M\omega_{ax}^2 x_m^2(t) + \sum_{n \neq m=1}^N \frac{Z^2 e^2}{4\pi\epsilon_0} \frac{1}{|x_n^2(t) - x_m^2(t)|}. \quad (2.28)$$

Now let's use the decomposition from the equation (2.27). Equilibrium positions can be obtained from

$$\left[\frac{\partial V}{\partial x_m} \right]_{x_m=x_m^{(0)}} = 0. \quad (2.29)$$

Defining the length scale l as

$$l^3 = \frac{Z^2 e^2}{4\pi\epsilon_0 M \omega_{ax}}, \quad (2.30)$$

we obtain the equation for the dimensionless equilibrium position u_m :

$$u_m - \sum_{n=1}^{m-1} \frac{1}{(u_n - u_m)^2} + \sum_{n=m+1}^N \frac{1}{(u_n - u_m)^2} = 0. \quad (2.31)$$

This system can be solved numerically for arbitrary N . The solutions for $N = 2..10$ depicted on the figure 2.8.

N	Scaled equilibrium positions									
2		-0.62996	0.62996							
3		-1.0772	0	1.0772						
4		-1.4368	-0.45438	0.45438	1.4368					
5		-1.7429	-0.8221	0	0.8221	1.7429				
6		-2.0123	-1.1361	-0.36992	0.36992	1.1361	2.0123			
7		-2.2545	-1.4129	-0.68694	0	0.68694	1.4129	2.2545		
8		-2.4758	-1.6621	-0.96701	-0.31802	0.31802	0.96701	1.6621	2.4758	
9		-2.6803	-1.8897	-1.2195	-0.59958	0	0.59958	1.2195	1.8897	2.6803
10	-2.8708	-2.10003	-1.4504	-0.85378	-0.2821	0.2821	0.85378	1.4504	2.10003	2.8708

Figure 2.8: A dimensionless equilibrium positions for $N = 2..10$ ions (along axial axis), defined as $u_m = x_m/l$ with l from the equation (2.30).

From this a formula for minimum spacing between ions is derived:

$$x_m^{(0)} \approx \left(\frac{Z^2 e^2}{4\pi\epsilon_0 M \omega_{ax}} \right)^{\frac{1}{3}} \frac{2.018}{N^{0.559}}. \quad (2.32)$$

2.3.2 Normal modes

Let's now consider nonequilibrium motion $q(t)$ from (2.27). The Lagrangian expansion of motion to the $O(q^3)$ term is

$$L = \frac{M}{2} \sum_{m=1}^N \dot{q}_m^2 - \frac{1}{2} \sum_{n,m=1}^N q_n q_m \left[\frac{\partial^2 V}{\partial q_n \partial q_m} \right]_{q_n=q_m=0}. \quad (2.33)$$

The partial derivatives are calculated explicitly, leading to the following Lagrangian form:

$$L = \frac{M}{2} \left[\sum_{m=1}^N \dot{q}_m^2 - \omega_{ax}^2 \sum_{n,m=1}^N A_{nm} q_n q_m \right], \quad (2.34)$$

where

$$A_{nm} = \begin{cases} 1 + 2 \sum_{p=1}^N \frac{1}{|u_m - u_p|^3} & \text{if } m = n, \\ \frac{-2}{|u_m - u_p|^3} & \text{if } m \neq n. \end{cases} \quad (2.35)$$

Since the A_{nm} matrix is real, symmetric and non-negative, its eigenvalues must be non-negative. Therefore the eigenvectors \mathbf{b} are defined as

$$\sum_{n=1}^N A_{nm} b_n^{(p)} = \mu_p b_m^{(p)}, \quad (2.36)$$

where $p = 1..N$, and μ_p are called curvatures. The eigenvectors are normalized to the 1. This task is solved numerically for an arbitrary N . For the 2..5 ions the eigenvectors are depicted on the figure 2.9.

With that we define normal modes as

$$Q_p(t) = \sum_{m=1}^N b_m^{(p)} q_m(t). \quad (2.37)$$

In this notation, the Lagrangian is rewritten as

$$L = \frac{M}{2} \sum_{p=1}^N \left[\dot{Q}_p^2 - \nu_p^2 Q_p^2 \right], \quad (2.38)$$

Eigenvalue			Eigenvector	
N=2	1	(-0.7071, 0.7071)		
	3	(-0.7071, 0.7071)		
N=3	1	(-0.5774, 0.5774, 0.5774)		
	3	(-0.7071, 0, 0.7071)		
	5.8	(0.4082, -0.8165, 0.4082)		
N=4	1	(0.5, 0.5, 0.5, 0.5)		
	3	(-0.6742, -0.2132, 0.2132, 0.6742)		
	5.81	(0.5, -0.5, -0.5, 0.5)		
	9.308	(-0.2132, 0.6742, -0.6742, 0.2132)		
N=5	1	(0.4472, 0.4472, 0.4472, 0.4472, 0.4472)		
	3	(-0.6395, -0.3017, 0, 0.3017, 0.6395)		
	5.818	(0.5377, -0.2805, -0.5143, -0.2805, 0.5377)		
	9.332	(-0.3017, 0.6395, 0, -0.6395, 0.3017)		
	13.47	(0.1045, -0.4704, 0.7318, -0.4704, 0.1045)		

Figure 2.9: A dimensionless axial normal modes of the ion chain. The normal modes' frequencies are scales to the curvatures according to (2.39).

where the normal mode axial frequency is

$$\nu_p = \sqrt{\mu_p} \omega_{ax}. \quad (2.39)$$

This analysis shows that the normal modes are uncoupled, and are self oscillations of the ion chain. This is a key object for trapped-ion quantum computing, as the laser-ion interactions must now be applied to the system as a whole.

For radial motion in the trap, the analysis is similar, with slightly different results for the A_{nm} matrix, which is now denoted as B_{nm} :

$$B_{nm} = \begin{cases} 1 - \sum_{p=1}^N \frac{1}{|u_m - u_p|^3} & \text{if } m = n, \\ \frac{1}{|u_m - u_p|^3} & \text{if } m \neq n. \end{cases} \quad (2.40)$$

The radial frequencies of the trap are typically much higher than axial, so the normal frequencies of radial modes are separated in spectrum from axial modes. However, it is possible for them to mix for the trap with comparable radial and axial trap frequencies (see the figure 2.10 a)).

For gates implementation usually the axial normal modes are used, due to the higher fidelity of operations^[25], however the radial modes also can be used, allowing faster gates with fewer motional heating.

2.3.3 Quantization and coupling

Let's move to quantum mechanics to describe the importance of the normal modes. The canonical conjugate momentum for Q_p is $P_p = M\dot{Q}_p$, and the Hamiltonian of the ion chain is

$$\hat{H} = \frac{1}{2M} \sum_{p=1}^N P_p^2 + \frac{M}{2} \sum_{p=1}^N \nu_p^2 Q_p^2. \quad (2.41)$$

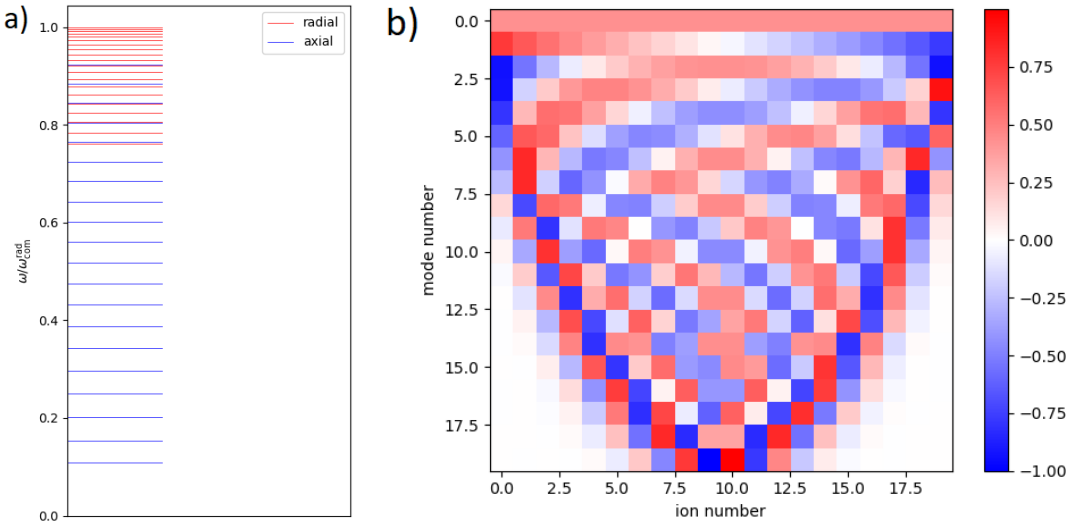


Figure 2.10: a) Normal modes spectrum as a relation $\omega/\omega_{COM}^{rad}$. b) An interaction matrix of normal modes. The color of the cell represents an interaction force of i^{th} ion with j^{th} mode. Here it can be clearly seen, how the COM mode (number 0) is uniform for all ions in the trap.

The second quantization for Q_p and P_p can be performed as

$$\hat{Q}_p = i\sqrt{\frac{\hbar}{2M\nu_p}}(\hat{a}_p - \hat{a}_p^\dagger), \quad (2.42)$$

$$\hat{P}_p = \sqrt{\frac{\hbar M \nu_p}{2}}(\hat{a}_p + \hat{a}_p^\dagger), \quad (2.43)$$

with creation and annihilation operators being responsible for p-mode excitation. In this notation, the displacement operator for the ion coordinate \hat{q}_m is represented as

$$\hat{q}_m(t) = \sum_{p=1}^N b_m^{(0)} \hat{Q}_p(t) = i\sqrt{\frac{\hbar}{2M\omega_{ax}N}} \sum_{p=1}^N M_{mp} (\hat{a}e^{-i\nu_p t} - \hat{a}^\dagger e^{i\nu_p t}). \quad (2.44)$$

Here, the M_{mp} is an interaction matrix between mth ion and pth normal mode:

$$M_{mp} = \frac{\sqrt{Nb_m^{(p)}}}{\nu_p^{1/4}}. \quad (2.45)$$

The interaction matrix allows one to determine, whether an ion "feels" the normal mode, and to choose the operational mode for laser-ion interaction application. On the figure 2.10 b) the normalized matrix is shown.

For the "center of mass" (COM) mode with $p = 0$ the interaction is uniform for all ions, which is preferable for quantum gates implementation. However, the COM mode is vulnerable to noise, which is a big problem for surface traps^[26]. Instead, a "breathing mode" ($p = 1$), where the interaction is proportional to the distance from the chains' center, is robust to the noise, but has a small interaction for the central ions. These problems have to be taken into account before mode's choice.

$$\chi_{i,j} = F(\eta_{i,m}\eta_{j,m}) \quad (2.46)$$

Chapter 3

Simulation of Surface Traps

This chapter deals with the simulation of potential distribution in the surface electrode trap via Python. In section 3.1 an overview of the theory behind the simulation process is given. The section 3.2 describes the "modeling of 2D ion traps (m2DIT)" package, covering the necessary parameters for the trap design. The package is registered as a patent by the Russian Quantum Center.

3.1 Analytic model of a surface trap

In section 2.1 differences in surface trapping of ions are briefly discussed. In this section we discuss surface traps in detail.

3.1.1 Ion motion near potential minima

The main difference from the conventional 3D Paul traps is a complicated potential distribution, due to which SETs are mainly analyzed numerically. However, we will see that it is possible to consider the potential near minimum as a harmonic one.

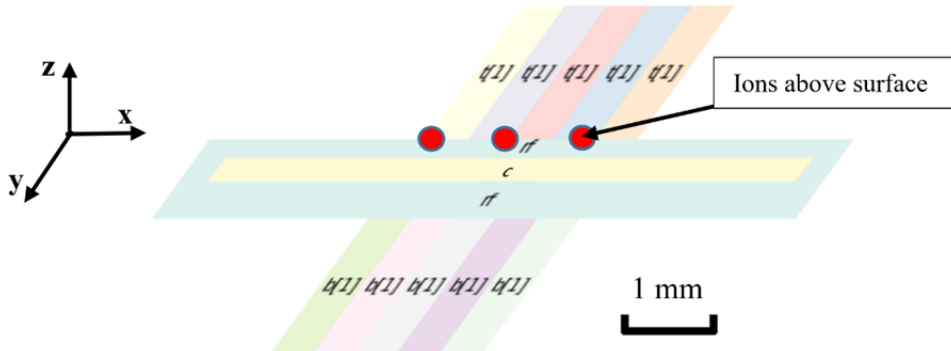


Figure 3.1: The simplest five-wire planar trap. Obtained by mapping 3D Paul trap on the surface, the pseudopotential distribution is trapping ions (red dots) above the surface. Here the RF electrodes are labeled as "rf", and other electrodes, being DC, are used for axial confinement and compensation. The same coordinate axes are used from now on.

Let's consider the surface electrode trap, such as on figure 3.1. The general field above the trap is represented by the potential^[27]:

$$\phi(x,y,z,t) = \phi_{DC}(x,y,z) + \phi_{RF}(x,y,z) \cos \Omega t, \quad (3.1)$$

for the trap with the RF frequency Ω . Here, $\phi_{DC} = \sum_{i=1}^{N_{DC}} \phi_{DC}^i$ – a sum of the potentials from every DC electrodes (same for ϕ_{RF}).

We will use the same notation, as in the section 2.3, considering small perturbations from the equilibrium positions (eq. 2.27). Near minimum, the potential can be expanded to it's first approximation $O(q^3)$:

$$\phi(q_x, q_y, q_z, t) = \frac{1}{2} \sum_{i,j=1}^N \left[\frac{\partial^2 \phi_{DC}}{\partial q_i \partial q_j} \right]_{q_i=q_j=0} q_i q_j + \frac{1}{2} \cos \Omega t \sum_{i,j=1}^N \left[\frac{\partial^2 \phi_{RF}}{\partial q_i \partial q_j} \right]_{q_i=q_j=0} q_i q_j, \quad (3.2)$$

where $i, j = x, y, z$. Then, for the equation of an ion motion we obtain:

$$M \frac{d^2 q_i}{dt^2} = -Ze \sum_j \left(\left[\frac{\partial^2 \phi_{DC}}{\partial q_i \partial q_j} \right] + \left[\frac{\partial^2 \phi_{RF}}{\partial q_i \partial q_j} \right] \cos \Omega t \right) q_j. \quad (3.3)$$

This equation can be denoted to the standard Mathieu equation:

$$\frac{d^2 \mathbf{q}}{d\tau^2} + [A + 2Q \cos 2\tau] \mathbf{q} = 0, \quad (3.4)$$

where A and Q are the Mathieu matrices – an extension of stability parameters a and q for a 3D equation:

$$A_{ij} = \frac{4Ze}{M\Omega^2} \left(\frac{\partial^2 \phi_{DC}}{\partial q_i \partial q_j} \right), \quad Q_{ij} = \frac{2Ze}{M\Omega^2} \left(\frac{\partial^2 \phi_{RF}}{\partial q_i \partial q_j} \right). \quad (3.5)$$

This equation can be separated into three independent equations only if A and Q commute, so they both can be diagonalized in the same basis. This can be done in symmetrical axial axis traps, such as conventional 3D traps. However it's not generally the case, which will be described in the section 3.1.6 in detail.

If the equations of motion are not separable, they can be analyzed by the multidimensional Floquet theory^[28]. The equation 3.4 is then rewritten in the first order system of ODE: $\dot{\mathbf{u}} = F(\tau)\mathbf{u}$, where

$$\mathbf{u} = \begin{pmatrix} q \\ \dot{q} \end{pmatrix}, \quad F(\tau) = \begin{pmatrix} 0 & I \\ A + 2Q \cos 2\tau & 0 \end{pmatrix}. \quad (3.6)$$

Then, since $F(\tau)$ is periodic with a period π , the equation will have independent solutions

$$\mathbf{u}_i(\tau) = e^{\mu_i \tau} \mathbf{b}_i(\tau), \quad (3.7)$$

which come at pairs of characteristic exponents $\pm \mu_i$. They are determined by the numerical integration of the equation

$$\dot{U}(\tau) = F(\tau)U(\tau), \quad (3.8)$$

with $U(0) = I$. Then, if λ_i is an eigenvalue of $U(\pi)$, then

$$\mu_i = \frac{\ln \lambda_i}{\pi}. \quad (3.9)$$

From the (3.7) it is clear that if the real part of $\mu_i \neq 0$, either + or - solution produces a motional mode, exponentially growing at time. So the stability criterion is that $\text{Im}(\mu_i) = 0$. Then the factor $\exp(\mu_i)\tau = \exp(i\beta_i\tau)$ describes an oscillation with the frequency

$\omega_i = \beta_i \Omega / 2$ which is a secular motion of ion in the trap, and is called a Mathieu mode. The solution (3.7) can be expanded to the Fourier series:

$$\mathbf{u}(t) = e^{\mu\tau} \sum_{n=-\infty}^{\infty} \mathbf{b}_n e^{2in\tau}. \quad (3.10)$$

For the stable motion \mathbf{b}_n represents the amplitudes of motional modes, starting from the lowest frequency – secular motion. The higher order modes are called micromotion, and for the $\beta \ll 1$, which basically means $\omega_{x,y,z} \ll \Omega$, the following relation is achieved: $b_0 \gg b_{\pm 1} \gg b_{\pm 2}$. With this, the pseudopotential approximation is valid:

$$\psi(x,y,z) = \frac{Z^2 e^2}{4M\Omega^2} |\nabla \phi_{RF}|^2. \quad (3.11)$$

Then the full trapping potential is $\Psi = \psi + \phi_{DC}$. For the pseudopotential approximation, since micromotion is neglected, the motion is considered secular, with the frequencies obtained from the field curvatures^[29]:

$$curv_{\alpha} = \text{Eig} \left(\frac{\partial^2 \Psi}{\partial q_i \partial q_j} \right), \quad (3.12)$$

$$\omega_{x,y,z} = \sqrt{\frac{Ze}{M} curv_{\alpha}}, \text{ [Hz]}, \quad (3.13)$$

where $\text{Eig}(\cdot)$ represents the eigenvalue of the matrix, $\alpha = [x,y,z]$. Then, the eigenvectors of the full potential hessian represent the directions of the oscillations with frequencies $\omega_{x,y,z}$. That means, that these directions can be rotated for asymmetrical potentials.

3.1.2 Potential distribution above the surface

To continue analysis it is necessary to obtain the analytical form of the potential. Assume, the electrodes are placed on the $z = 0$ plane. Then, for the electrostatic potential ϕ in the free-space region above the surface, the Laplace equation is valid:

$$\nabla^2 \phi = 0. \quad (3.14)$$

The following calculations are performed in **gapless** and **infinite electrodes** approximations. For the latter, the electrodes are assumed to collectively occupy the whole $z = 0$ plane, and the potential drops to zero with $x,y \rightarrow \pm\infty$. This approximation is appropriate, because it just means that the trap itself lies on the infinite grounded conducting plane. The trap size (~ 10 mm) is usually \gg than the size of a harmonic region of the trap ($\sim 100\mu\text{m}$).

The gapless approximation implies the absence of the gaps between electrodes. Its reliability will be discussed at the end of section 3.1.3.

The stated task is a boundary-value problem. It's general solution given the boundary conditions:

$$\begin{aligned} \phi(x,y,z) = & \int_0^{\infty} dk_y \int_0^{\infty} dk_x e^{-\sqrt{k_x^2+k_y^2}z} [A_1(k_x,k_y) \cos(k_x x) \cos(k_y y) \\ & + A_2(k_x,k_y) \sin(k_x x) \cos(k_y y) + A_3(k_x,k_y) \cos(k_x x) \sin(k_y y) \\ & + A_4(k_x,k_y) \sin(k_x x) \sin(k_y y)]. \end{aligned} \quad (3.15)$$

Here A_i are the degrees of freedom of the equation, which are determined for the certain electrode geometry. Generally two geometries are identified, depending on the electrode's

shape. Point traps consist of the electrodes with circle form. This geometry is useful, because it can approximate an arbitrary electrode shape, with infinitesimal circles. However, this is computationally more challenging.

Polygonal traps consist of the rectangular electrodes. This is a more common trap geometry, due to the simpler fabrication and operation. All SETs in this diploma are polygonal.

Consider a rectangular electrode with the applied voltage V on the infinite grounded plane. If the two opposite vertices of the electrode have coordinates $(x_1, y_1, 0)$ and $(x_2, y_2, 0)$, a respective boundary condition is given:

$$\phi(x,y,0) = \begin{cases} V, & x_1 < x < x_2 \wedge y_1 < y < y_2, \\ 0, & \text{otherwise.} \end{cases} \quad (3.16)$$

Then, the degrees of freedom are calculated by taking a Fourier transform of the function:

$$\begin{aligned} A_1(k_x, k_y) &= \frac{1}{\pi^2} \int_{-\infty}^{\infty} dy \int_{-\infty}^{\infty} dx \phi(x,y,0) \cos(k_x x) \cos(k_y y) \\ &= \frac{1}{\pi^2} \int_{y_1}^{y_2} dy \int_{x_1}^{x_2} dx V \cos(k_x x) \cos(k_y y) \\ &= \frac{V}{\pi^2 k_x k_y} [\sin(k_x x_2) - \sin(k_x x_1)] \times [\sin(k_y y_2) - \sin(k_y y_1)]. \end{aligned} \quad (3.17)$$

The similar equations are obtained for other A_i . Then, substituting them to the (3.15) we obtain:

$$\begin{aligned} \phi(x,y,z) &= \frac{V}{\pi^2} \int_0^{\infty} dk_y \int_0^{\infty} dk_x \frac{e^{-\sqrt{k_x^2 + k_y^2} z}}{k_x k_y} \{ \sin[k_x(x_2 - x)] \\ &\quad - \sin[k_x(x_1 - x)] \} \{ \sin[k_y(y_2 - y)] - \sin[k_y(y_1 - y)] \}. \end{aligned} \quad (3.18)$$

Taking the integral, we finally determine the analytic potential:

$$\begin{aligned} \phi(x,y,z) &= \frac{V}{2\pi} \left\{ \tan^{-1} \left[\frac{(x_2 - x)(y_2 - y)}{z\sqrt{z^2 + (x_2 - x)^2 + (y_2 - y)^2}} \right] \right. \\ &\quad - \tan^{-1} \left[\frac{(x_1 - x)(y_2 - y)}{z\sqrt{z^2 + (x_1 - x)^2 + (y_2 - y)^2}} \right] \\ &\quad - \tan^{-1} \left[\frac{(x_2 - x)(y_1 - y)}{z\sqrt{z^2 + (x_2 - x)^2 + (y_1 - y)^2}} \right] \\ &\quad \left. + \tan^{-1} \left[\frac{(x_1 - x)(y_1 - y)}{z\sqrt{z^2 + (x_1 - x)^2 + (y_1 - y)^2}} \right] \right\}. \end{aligned} \quad (3.19)$$

Using this formula an arbitrary set of rectangular electrodes may be calculated as a sum of such potentials. On the figure 3.2 a potential from two RF electrodes is shown. It demonstrates a trapping tube for radial ion trapping. On the y-z plane the potential minimum is clear. In the upper side of the picture a so-called saddle point is seen. It is the lowest potential bound for the ion. The difference between the potential minimum and saddle point potential is called **trap depth**. It shows the minimum kinetic energy for ions to escape the trap. The calculation of the trap depth is performed numerically, and is an important parameter for evaluating trap capabilities.

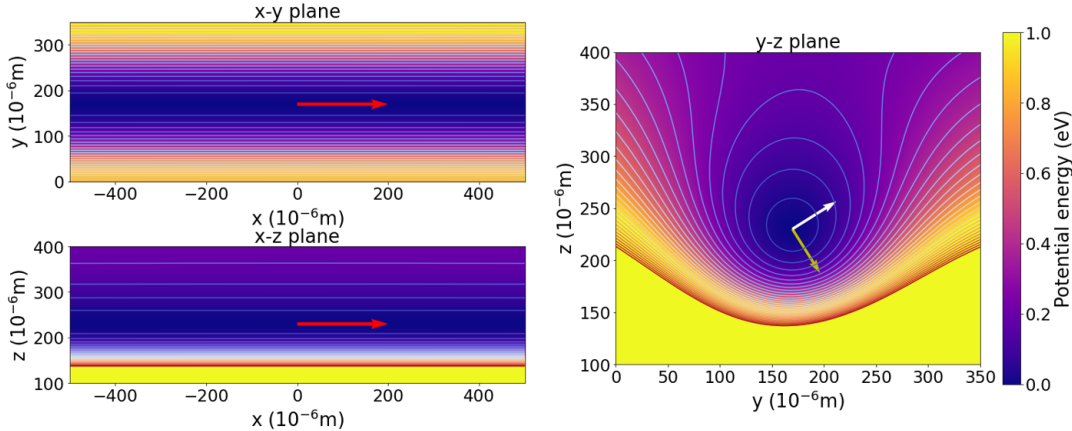


Figure 3.2: A pseudopotential distribution, demonstrating a potential tube to trap ions. Here, the labeled pics represent cross-sections in respective planes, coming through the potential minimum. The coordinate axes are similar to 3.1. The potential distribution is obtained for the researched trap using the m2DIT package, which will be further discussed in the section 3.2.1.

3.1.3 Gapless approximation

In the realistic surface trap design the insulating gaps between electrodes are necessary for them to hold different voltages. In the gapless approximation, discussed above, their influence is, however, neglected. Usually the gaps' size \ll the electrodes' scale, and is about $10 \mu\text{m}$. Several gap models are considered in the literature, but they all prove the neglectful influence to the whole potential even in the extreme cases of gap size comparable to the electrode's^{[27][30]}.

For the rectangular shape, the gaps are considered straight, with the linearly varying potential along the gap's width. The analysis shows an accuracy of $> 98\%$ for the gapless approximation. The most precision is achieved by extending both electrodes, separated by the gap, to the gap's center. This procedure is implemented for all diploma simulations.

For the point traps the effects of gap are limited by the 5%. The procedure to minimize the effects by extending electrodes is slightly different, and expressed in detail in [30].

3.1.4 Cover plate influence

In the previous research we considered an infinite free-space over the electrode surface. In practice, however, the trap is placed in the vacuum chamber, and is surrounded by insulating parts of the experimental setup. This leads to the possibility of an external influence such as a field bias from polarized insulators. For this purpose SETs are usually shielded by the cover conductive plane or a mesh electrode. This shielding not only eliminates an unwanted bias, but proved to significantly increase the trap depth of the trap^[31].

The general method for calculating the effects of the imaging charges is to analyze Green functions^[32]. The total Coulomb energy for ions Q_i in the trap with cover plane placed on the height $z = H$:

$$E_C = \frac{1}{4\pi\epsilon_0} \left[- \sum_i Q_i^2 e_H(z_i) + \sum_{i < j} Q_i Q_j G_H(r_i, r_j) \right], \quad (3.20)$$

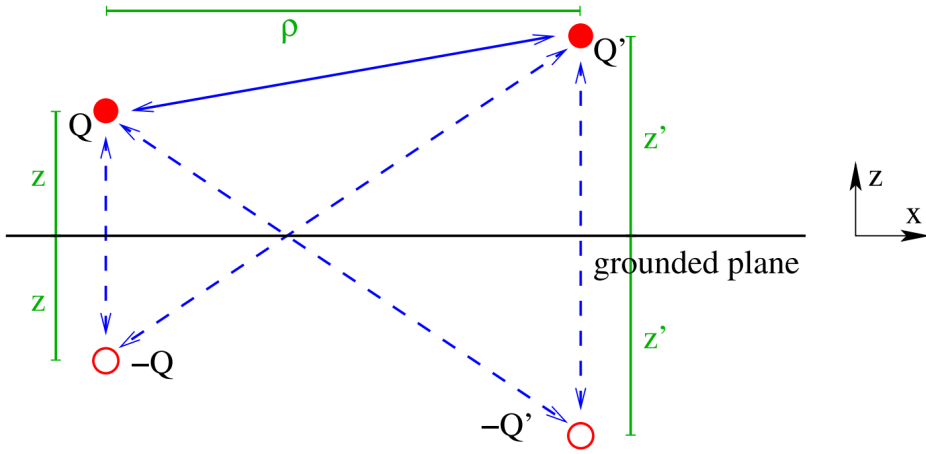


Figure 3.3: The mirroring effect of the covering conductive plane. ions interact not only with each other, but also with their images. Figure courtesy of [32].

where e_H is a scaled self-potential, and G_H is a Green function. Both are found by summing over the infinite sequence of mirroring planes, which appear periodically with heights $h = mH$, where m is an expansion of which we consider the cover electrode. The Green function modifies the interaction between ions with the presence of a cover. In the diploma this modification is neglected, since effects become relevant only for far-away placed ions, where the distance between them is $\gg h$ – an ion height.

The influence of cover is more relevant for the self potential distribution. According to the method of images, the full potential for the particle with the coordinates (x,y,z) in the trap with electrostatic potential $\psi(\mathbf{r})$ (without cover):

$$\Psi(x,y,z) = \sum_{m=-\infty}^{\infty} \psi(x, y, z + 2mH). \quad (3.21)$$

Due to the fact, that $\psi(\mathbf{r})$ vanishes with $z \rightarrow \pm\infty$, for the practical calculations the sum is bounded by the max number of an expansion m_{max} . For the simulations, performed in this diploma, $m_{max} = 5$.

3.1.5 Micromotion compensation

Describing ion motion near potential minimum, we introduced the micromotion as an additional motional modes with higher frequencies, caused by the displacement of the ion from the RF minimum (see figure 3.4). This motion is undesirable for several reasons. Due to the Doppler effect from the ion's motion, it changes the transition lines. For the Doppler cooling it broadens the $S_{1/2}$ - $P_{1/2}$ transition, therefore reducing Doppler cooling efficiency. In the resolved sideband regime micromotion forms self sidebands, which decrease the coupling strength to the laser for necessary transitions^[19]. Due to these reasons, it's necessary to compensate micromotion.

The most general way is to reduce the displacement of an ion due to electrostatic DC fields. It can be achieved by applying compensation voltages to the additional electrodes. This is one of the reasons for an interest towards surface traps – there can be an arbitrary number of electrodes, which increases the freedom degrees of the system to compensate micromotion.

This is also useful, because in the experimental setup there are unpredictable stray electrical fields with undetermined sources. Stray fields are also moving ions away from

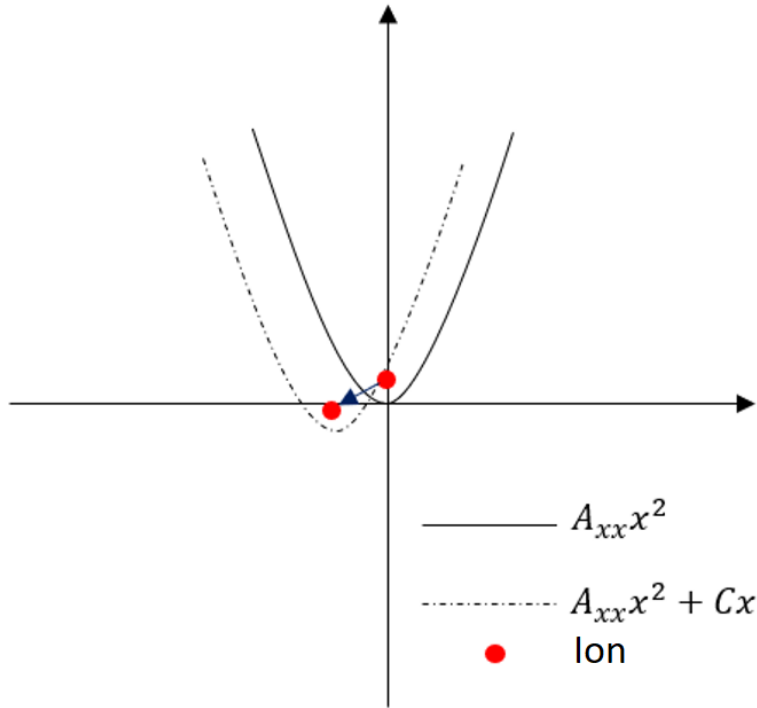


Figure 3.4: The displacement of the ion position, depending on the applied DC voltage.

The solid line shows an axial confinement potential, the dashed line shows the displacement of the potential due to the electrostatic field.

the RF minimum, and additional electrodes compensate them. However, these effects in principle can't be simulated, and are implemented experimentally depending on the flowing measurements.

However it needs to be considered in voltage designing. Application of DC voltage set accomplishes two things – implementation of axial confinement and zero displacement of the potential minimum.

The task to find the voltages comes down to the optimization task for a V_i set:

$$\text{minimize: } \sum_i V_i^2, \quad (3.22)$$

$$\sum_i V_i \nabla \phi_i = 0, \quad (3.23)$$

$$\sum_i V_i \frac{\partial^2 \phi_i}{\partial x^2} = \frac{m\Omega^2}{4Ze} A_{xx}. \quad (3.24)$$

Here the first term is minimizing an applied voltages, the second term sets the displacement to 0, and the last equation defines the axial confinement, as A_{xx} is an axial curvature of the DC potential. This task is implemented in the m2DIT package.

3.1.6 Stability analysis

Let's return to equation 3.4. As it was mentioned, this equation is only separable for a symmetric potential distribution, when A and Q commutes. However, in surface traps it is favorable to induce asymmetric potential. For successful cooling, all 3 secular motional modes need to be addressable. Usually the optical-laser system in surface traps is parallel

to the surface. If the potential is symmetric, the motional modes are parallel to the coordinate axis, so z -mode will be uncoupled with lasers. Because of that, the slight asymmetry is induced, which rotates motional modes for them to all be accessible through the laser system. The angle of rotation is then determined through the modes' directions from (3.12).

In the diploma this asymmetry is achieved by difference in the width of two RF electrodes in the five-wire geometry. General way to analyze stability is discussed in section 3.1.1. However, it is useful to obtain the stability region for the trap to simplify design. In the m2DIT package the method from [33] is implemented.

Consider A and Q matrices. If the RF and DC minimums coincide, the A and Q matrices must be non-negative and traceless, as a hessian of the potential in minimum.

For the traps with long RF electrodes, such as a researched trap in diploma, the axial motion can be approximately decoupled from the radial y - z motion. With this, only the coupled modes are considered, reducing A and Q matrices' dimensions to 2. For the ion motion to be confined axially, the $A_{xx} > 0$, so the trace of the reduced matrix \tilde{A} is negative. And for the approximation to be valid, the RF potential along x -axis must be neglectful, so the reduced \tilde{B} is traceless. In their respective coordinates they now are denoted as:

$$\tilde{A} = a \begin{pmatrix} 1 & 0 \\ 0 & -\alpha \end{pmatrix}, \quad \tilde{Q} = q \begin{pmatrix} 1 & 0 \\ 0 & -1 \end{pmatrix}. \quad (3.25)$$

Then the introduced a-q parameters are the stability parameters of an asymmetrical trap. The θ is an angle between two coordinate systems, diagonalizing \tilde{A} and \tilde{B} . If B_A , B_Q – respective transition matrices to these coordinates, the equation for θ :

$$\begin{pmatrix} \cos(\theta) & \sin(\theta) \\ \sin(\theta) & -\cos(\theta) \end{pmatrix} = B_Q^{-1} B_A. \quad (3.26)$$

We denote $\cos(2\theta) = c$, $\sin(2\theta) = s$. Then, we obtain the coupled Mathieu system:

$$\begin{aligned} \ddot{y} + ay + 2q(cy + sz) \cos 2\tau &= 0, \\ \ddot{z} - a\alpha z + 2q(sy - cz) \cos 2\tau &= 0. \end{aligned} \quad (3.27)$$

The stability of the system is analyzed by the method of multiple scales. In result, the equations of curves, bounding the stability region are obtained:

$$a_1 = -\frac{q^2}{2}, \quad (3.28)$$

$$a_2 = \frac{q^2}{2\alpha}, \quad (3.29)$$

$$a_3 = 1 - cq - \left(\frac{c^2}{8} + \frac{2s^2(5 + \alpha)q^2}{(1 + \alpha)(9 + \alpha)} \right), \quad (3.30)$$

$$a_4 = -\frac{1}{\alpha} \left(1 - cq - \left(\frac{c^2}{8} + \frac{2s^2(5 + 1/\alpha)q^2}{(1 + 1/\alpha)(9 + 1/\alpha)} \right) \right). \quad (3.31)$$

This analysis is implemented in the m2DIT package. The stability region is depicted on figure 3.5 for the researched trap.

However these are boundary curves for a primary stability region. For asymmetric traps an existence of the secondary, much larger stability region is predicted^[33] for $\theta = 45^\circ$. This result isn't researched in the diploma, but is one of the directions for the future work.

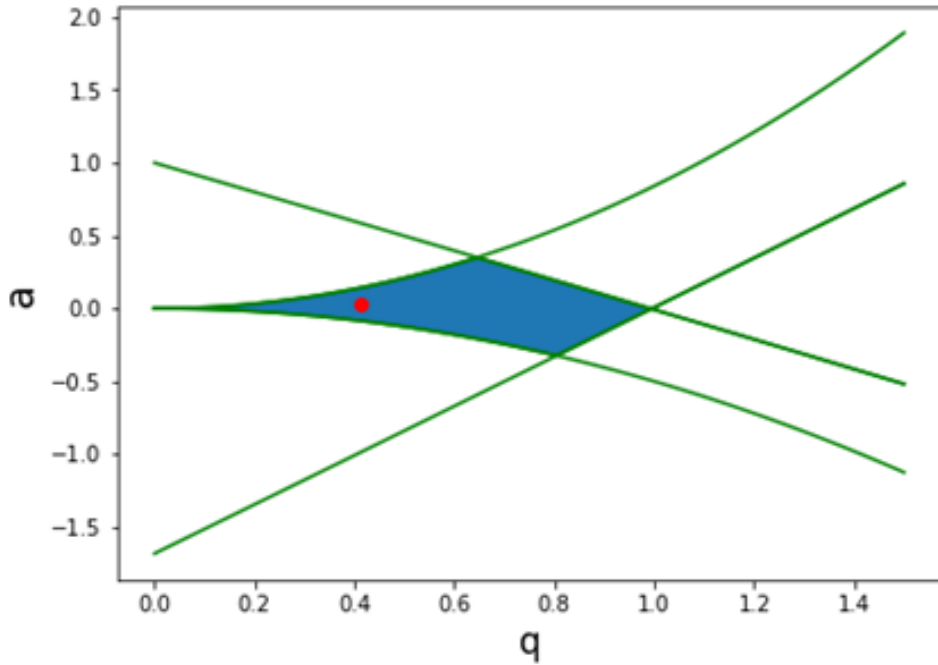


Figure 3.5: A stability diagram for an asymmetric surface trap. A blue space represents a stability region, and a red dot shows the position of our trap (in a - q coordinates). The picture was obtained by the m2DIT package.

3.2 Python simulation of SET

Due to the hard computational challenge in modeling planar electrodes, usually the simulation of surface traps is performed on the computer. There are several approaches on how to do that (see more in section 5.2). In this diploma all computations are performed via Python with the electrode package^[34]. This package allows us to simulate the potential distribution over the electrode's plane, and obtain surface trap's parameters. The m2DIT package is the extension of the aforementioned package.

3.2.1 Program description

The package m2DIT operates fully by the analytic model, described in section 3.1. First the trap geometry is defined. *FiveWireTrap()* function defines the geometry of the widely used five-wire trap, as depicted on the figure 3.6 a). It conveniently defines an arbitrary set of side DC electrodes and the cover electrode, and produces the file of coordinates for the gds-file formation. The gds-file is later sent for the manufacturing process.

Then the determination of RF minimum occurs. The potential form RF lines is pictured on the figure 3.2. The minimum is found using *scipy.optimize.minimize()* function from the Science Python (SciPy) package. It uses Newton method for minimization.

On the next step the DC voltage set for axial confinement is determined, according to the procedure in (3.22-3.24). This is implemented by the function *electrode.shims()* from the electrode package. The resulting voltages are depicted on the figure 3.6 b) for the researched geometry. The maximum DC voltage is 15 V, which is determined by the capacity of the frequency filters in the experimental setup. However, introducing additional electrodes allows to create strong confinement even with small individual voltage^[17].

The pseudopotential distribution is then depicted on the figure 3.7. The picture clearly indicates the trapping region, and the saddle point. The arrows represent secular

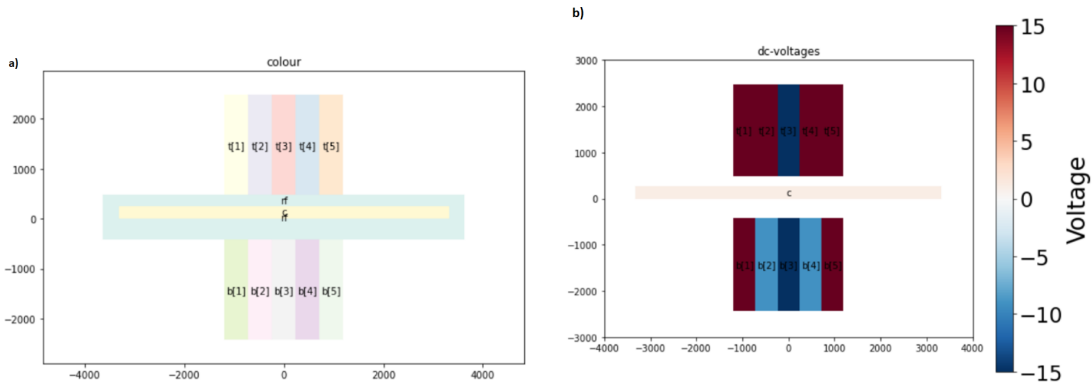


Figure 3.6: a) A trap layout. Here it is considered gapless. RF and central DC electrodes are labeled as "rf" and "c", and top and bottom DC electrodes are labeled as "t[i]", "b[i]". It is clear that RF lines are asymmetrical here. b) A layout of DC electrodes, with the color representing their voltage through the colorbar. The limiting voltage was 15 V.

modes' directions, and show the rotation along with an asymmetric potential.

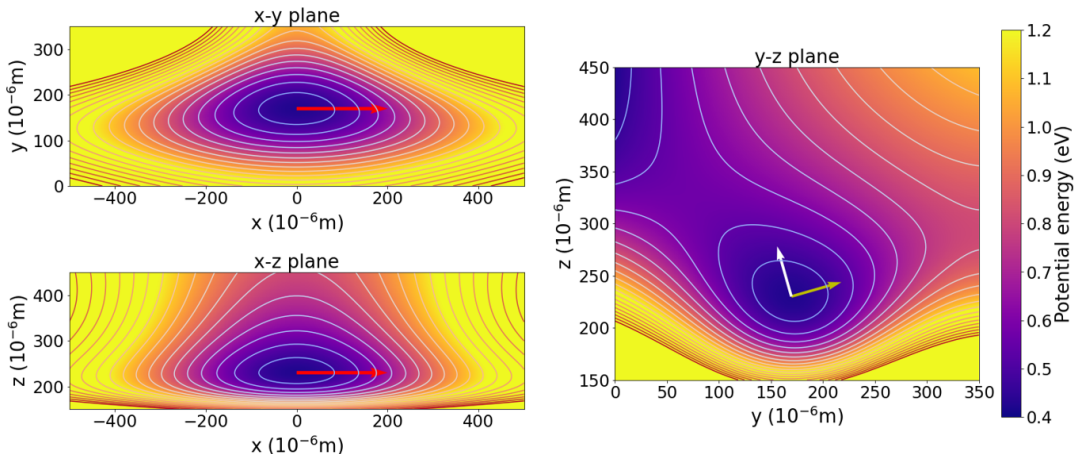


Figure 3.7: The full potential distribution above the considered trap's surface. The scheme is the same, as on the figure 3.2. The arrows represent the directions of the secular modes. The modes are clearly rotated by the asymmetry of the potential, which allows to cool the ion by the laser scheme, parallel to the surface.

But the pseudopotential well doesn't indicate the stability of the ion motion in the trap. The next step performs the procedure, described in section 3.1.6 to determine the stability region of the trap, and our stability parameters. For the researched geometry a figure 3.5 was obtained. It is seen that the trap's parameters lie in the stability region, and the motion is stable.

Then, the package demonstrates individual potentials from each electrode, which can be helpful for determining their role and following designing. Also it is a possible tool to determine the source of stray fields.

The next block determines the trap depth. The task to find the saddle point is complicated, for too shallow potentials it can't be achieved. The saddle point is searched as a point, where first derivatives of the pseudopotential equal to 0, and hessian of the potential is neither positive nor negative definite. The search is implemented by the

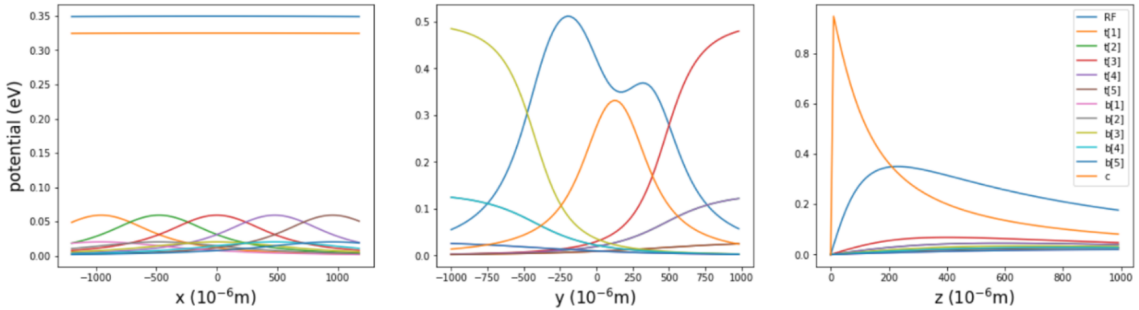


Figure 3.8: The individual potential distributions from each electrode. The figures represent distributions along x – axial, y – radial parallel to the surface, and z – vertical axes, passing the minimum point, respectively.

function `electrode.saddle()`. Due to the method restrictions, the starting point of the search has to be in the $50 \mu\text{m}$ radius from the real saddle point, which is determined by the plot of the distribution, such as 3.7.

The saddle point is searched by the rational function optimization method. In particular a modified Newton-Raphson method is used, where the hessian is approximated on each step using Bofill updates^[35].

The trap depth was found for the researched trap $\Delta\psi = 0.14 \text{ eV}$. On the figure 3.8 a plot of the potential obtained for the line, coming through both the minimum and the saddle point, is shown.

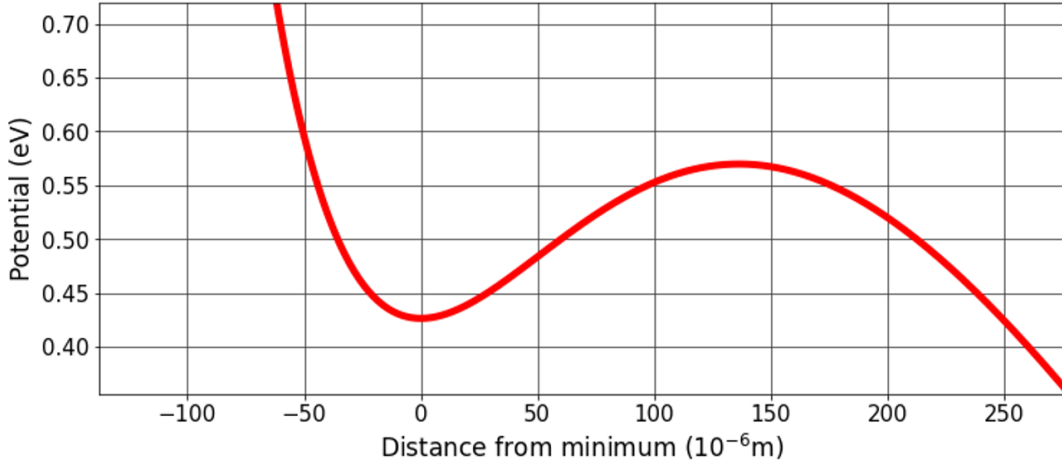


Figure 3.9: The plot of the potential distribution along the axis, going through the potential minimum and a saddle point.

Finally, the analysis of the ion motion near minimum is obtained with the function `electrode.analyze_static()`. The text is shown on the figure 3.10 for the researched trap. The function returns the necessary parameters, determining the trap's performance, such as potential in minimum, secular and Mathieu motional modes, and heating rate for the Mathieu modes, evaluated for the white, uncorrelated electrical noise on the electrodes. This parameter, however, is not representative, because the main source of heating in the surface traps is so-called anomalous heating^[36], which can't be properly evaluated on the simulation step.

```
parameters:
  f=17 MHz, m=40 amu, q=1qe, l=1 μm, scale=7.27 V'/V_SI
coordinates:
  analyze point: [-1.59e-04 1.70e+02 2.30e+02]
    ([ -1.59e-04 1.70e+02 2.30e+02] μm)
  minimum is at offset: [0. 0. 0.]
    ([0. 0. 0.] μm)
potential:
  dc electrical: 0.43 eV
  rf pseudo: 1.2e-09 eV
  saddle offset: [4.23 0.6 0.98]
    ([4.23 0.6 0.98] μm)
  saddle height: 0.00019 eV
force:
  dc electrical: [ 7.55e-19 1.30e-18 -1.66e-17] eV/l
    ([ 7.55e-13 1.30e-12 -1.66e-11] eV/m)
  rf pseudo: [ 2.37e-12 2.63e-07 -4.23e-07] eV/l
    ([ 2.37e-06 2.63e-01 -4.23e-01] eV/m)
modes:
  pp+dc normal curvatures: [1.27e-05 6.83e-05 1.18e-04]
  motion is bounded: True
  pseudopotential modes:
    a: 0.8825 MHz, [ 1.00e+00 -3.86e-07 -7.88e-07]
    b: 2.043 MHz, [ 1.55e-07 9.62e-01 -2.74e-01]
    c: 2.69 MHz, [ 8.63e-07 2.74e-01 9.62e-01]
    euler angles (rzxz): [ 180.      15.89 -180. ] deg
  mathieu modes:
    a: 0.8825 MHz, [ 9.95e-01 -3.84e-07 -7.83e-07]
    b: 2.106 MHz, [ 1.50e-07 8.88e-01 -2.53e-01]
    c: 2.794 MHz, [ 7.80e-07 2.47e-01 8.67e-01]
    euler angles (rzxz): [ 180.      16.24 -180. ] deg
heating for 1 nV2/Hz white uncorrelated on each electrode:
  field-noise psd: [1.07e-14 1.95e-13 1.35e-12] V2/(m2 Hz)
  a: ndot=1.745 /s, S_E*f=9.319e-09 (V2 Hz)/(m2 Hz)
  b: ndot=3.944 /s, S_E*f=1.2e-07 (V2 Hz)/(m2 Hz)
  c: ndot=62.88 /s, S_E*f=3.367e-06 (V2 Hz)/(m2 Hz)
```

Figure 3.10: The full analytic of the ion motion near the potential minimum. Here it can be seen that secular modes are in good agreement to the Mathieu modes, which emphasizes the validity of the pseudopotential approximation. Note that the result for saddle height is not accurate. This happens due to the specifics of the algorithm, discussed earlier. That is why the trap depth' calculation is performed independently.

3.2.2 Verification

For future work with the package, the verification was performed. As a reliable result, a geometry of the YK-3 trap, defined in the PhD thesis [17]. The trap is depicted on the figure 3.11 a), with all the sizes.

The trap voltages are shown on the table 3.1.

Table 3.1: The voltage set for YK-3 trap.

Electrode	L3	L4	L5	R3	R4	R5
Voltage (V)	5.4	-38	5.4	25.5	-29.3	25.5

The YK-3 was simulated by COMSOL, which is a powerful software for electromagnetic simulations. The results were experimentally proved to be reliable. The simulated potential distribution for YK-3 is shown on the figure 3.12 a). The calculated trap depth amounted to 35 meV.

The trap with the same geometry and characteristics (figure 3.11 b)) was simulated by the m2DIT package. The results are shown on the figure 3.12 b). The trap depth is calculated to be 41 meV.

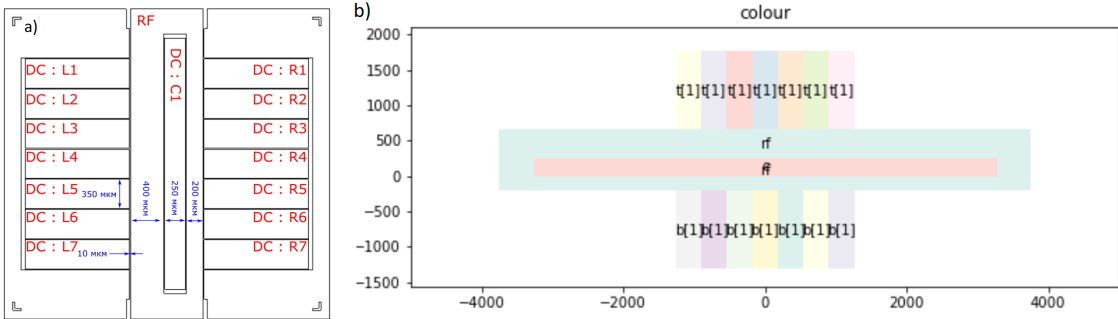


Figure 3.11: a) The YK-3 trap from [17]. The RF amplitude is 140 V, and frequency 20.6 MHz. b) A similar trap, generated by the m2DIT package. The sizes are now proportional.

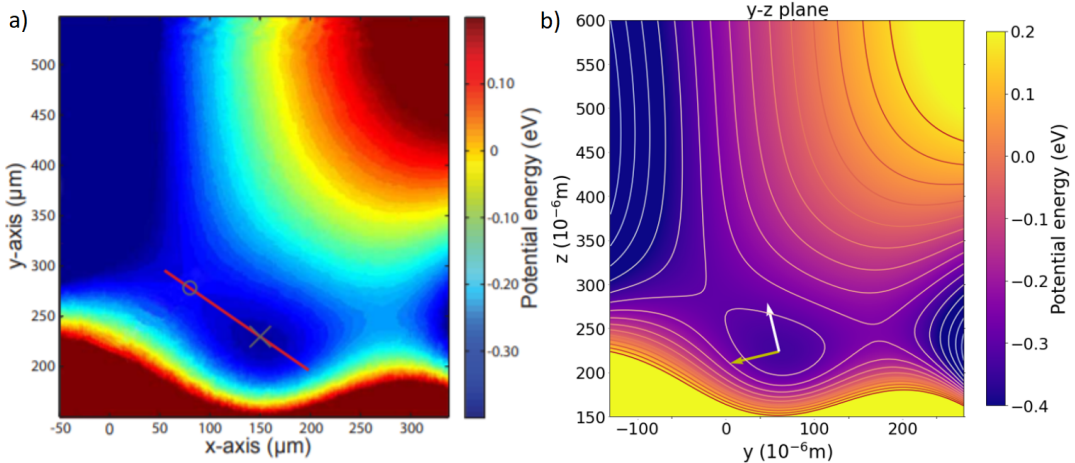


Figure 3.12: The potential distribution in the radial cross-section through the minimum.
a) For the YK-3 trap, obtained from COMSOL simulation. b) For the trap by the m2DIT package. It is clear, that they are similar (but mirrored).

For the whole distribution the accordance is great, but the trap depth is 15% higher, than in [17]. This can be explained by the method of simulation. COMSOL simulation doesn't use gapless or infinite electrode approximation^[37], and for the simulation the whole trap layout was used. The experimental trap consists not only of the trapping region (which is simulated by the m2DIT package), but also from the wires that conduct the potential to the electrodes (see figure 4.10). With that, the precision of the m2DIT package is smaller, but allows quick and convenient calculations for designing the trap.

3.2.3 Technical requirements

The package is working with Python 3 and higher. Additionally the C/C++ 11 and higher must be installed. And the electrode package must be installed.

An advantage of this package is a small requirement, so it can be executed on any modern laptop.

Chapter 4

Ion dynamics simulation in Surface Trap

In this chapter the simulation of ion dynamics in the planar trap is discussed. In section 4.1 an analytic model for ion dynamics simulation is provided. In section 4.2 the "Surface Ion Dynamics (SID)" Python package for the simulation is demonstrated. The package is in the process of patent registration in the RQC. In section 4.3 the research of phase transitions in Coulomb crystals was carried, using the SID package. In section 4.4 the verification of the package's functions is provided. The result of the work is presented in section 4.5 as a trap design for 5 ions.

4.1 Python modeling of ion motion

Since the analytic form of potential makes it almost impossible to derive an analytic trajectory, the ion dynamics is simulated numerically. This section provides an overview of the theory required for the simulation implementation.

4.1.1 Molecular Dynamics Method

The main method of simulating a classical behavior of the atomic particles is the Molecular Dynamics method (MD method). A basic algorithm for MD method is depicted on the figure 4.1^[38]. The main idea behind the method is numerical integration of Newton's classical equations of motion.

Consider N particles in the potential field $E_{pot}(\mathbf{x})$, which contains both an external potential, and an interaction potential between particles. We consider particles as dots with masses m_i . For the i^{th} particle, the equation of motion would be:

$$m_i \frac{d^2\mathbf{x}}{dt^2} = - \left(\frac{\partial E_{pot}(\mathbf{x})}{\partial \mathbf{x}} \right)_{\mathbf{x}=\mathbf{x}_i}. \quad (4.1)$$

Given a position $\mathbf{x}_i(t)$ in the moment t , the position within a very short moment Δt is determined by the Taylor's expansion (for a single coordinate):

$$x(t + \Delta t) = x(t) + \dot{x}(t)\Delta t + \ddot{x}(t) \frac{(\Delta t)^2}{2!} + \dots \quad (4.2)$$

This denotes the algorithm's idea – numerical integration of these equations of motion will produce the trajectories for a Δt timestep.

The simplest way will be to just assume the quadratic approximation in (4.2). However, this is a poor approximation in practical cases^[39]. Considering Newton's third law,

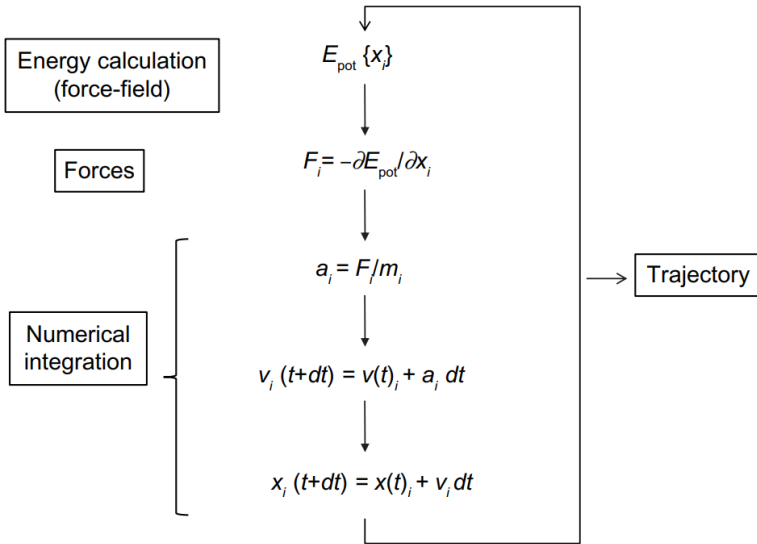


Figure 4.1: A basic algorithm for MD method. Here, the outputs are $3N$ trajectories for N particles in the potential energy field E_{pot} . Firgure courtesy of [38]

the net force affecting the system must be 0, thus conserving total momentum and energy of the system. But this simple approximation leads to the sufficient total energy fluctuations over the simulation time.

There are several methods for the improvement of this approximation. The LAMMPS software, used in the diploma, is using the Verlet algorithm^[40], applying the numerical integration with the fourth order precision (up to the $(\Delta t)^4$ term)^[41]. The integration process in this algorithm is then applied in the following sequence:

$$\mathbf{x}(t + \Delta t) = 2\mathbf{x}(t) - \mathbf{x}(t - \Delta t) + \mathbf{a}(t)(\Delta t)^2 + O((\Delta t)^4), \quad (4.3)$$

where \mathbf{a} is an acceleration from (4.1).

Langevin dynamics

Ions in the RF trap are considered to be cooled down after their confinement, thus condensing into Coulomb crystals. The natural method for implementing such cooling lies in the addition of Langevin dynamics to the simulation. The equation, describing the dynamics is given by the Langevin equation:

$$m_i \frac{d^2 \mathbf{x}}{dt^2} = F_i(\mathbf{x}) - \gamma_i \dot{\mathbf{x}} + f_i(t), \quad (4.4)$$

where F_i is a generalized force from (4.1), γ_i – friction coefficient, responsible for cooling, and f_i – a stochastic force, which represent degrees of freedom, not included in the simulation.

Constraints of the method

As stated in the (4.2), the MD method is approximated over the Taylor's expansion in the numerical integration. This irresistibly makes simulations mathematically ill-conditioned. With the increase in simulation time and a number of particles, the simulation will accumulate errors.

However for the trapped ion-case these concerns are not important. Modern MD simulations operate with 100'000 particles on a long time window. But trapped ion simulations are typically limited by hundreds of ions (for the present moment), and with the fast cooling speed. After the Coulomb crystal condensation, the classical simulation describes particles in equilibrium, and all the following processes, resulting in ion's losses, can't be pre-simulated.

The main approximation of the method is that the quantum effects on the dynamics are neglected. For ions in the RF trap this assumption must be applied carefully. Due to the fact that ions in the trap are condensed to the ground state temperature, the system exhibits a strong quantum behavior. However, the ion separation length is usually $\sim 1 \mu\text{m}$, which is big enough to consider ions' motion classically for the purpose of the simulation. The ions are simulated for the time period before their crystallisation, thus the quantum effects of the system can be neglected.

4.1.2 Surface trap case

The goal of ion dynamics simulation is to show their operation to determine the proper design for the trap. There are several results, obtainable through the direct simulation:

Ions' stability. Firstly, there is no analytic model to determine the stability of motion for many ions, so the general simulation shows if the ions will be confined in the trap. Now the consensus is that we need the trap with the a-q parameters lying deeply in the stability region^[42]. The theoretical research for this model is one of the directions for our following research.

Confinement of hot ions. Another detail regarding the trapping of several ions in the SET is the latter's low trap depth. For the general planar trap, the depth is about 0.1 eV, which is comparable with the ion's kinetic thermal energy. Because of this, it is challenging to trap more than 1 ion in such a trap^[26]. However, the ion's temperature may be reduced before trapping, using magneto-optical traps or optical tweezers. With that, the ion's temperature is low enough for the ion to be confined in SET. The simulation allows to define the ion's temperature in the trap, determining its ability to confine hot ions.

Parameters of Coulomb crystal. If ions are proved to be confined, the simulation gives the form of a condensed ion crystal. The final positions of the ions indicate the phase of the crystal (see section 4.3) and allow to obtain normal modes, important for following operation. And the ability to obtain trajectories of ions in the trap is necessary for the future research in *shuttling* – ion crystal's displacement with electrical fields, which is a prerequisite for trapped-ion quantum computer scaling^[15].

SET potential with many ions

In the case of planar traps, the time-dependent potential energy in (4.1) is given by the equation:

$$E_{pot}(x,y,z,t) = \sum_{i=1}^{N_{DC}} \phi_{DC}^i(x,y,z) + \sum_{i=1}^{N_{RF}} \phi_{RF}^i(x,y,z) \cos(\Omega t) + \sum_{n \neq m=1}^N \frac{Z^2 e^2}{4\pi\epsilon_0} \frac{1}{|\mathbf{r}_n - \mathbf{r}_m|^2}, \quad (4.5)$$

for N ions confined in the trap with N_{DC} DC electrodes and N_{RF} RF electrodes with the RF frequency Ω . Here, the ϕ^i is a polygon potential of the form (3.19). In this equation, the more general form of the time-dependent potential is used, instead of the pseudopotential approximation. This way a simulation will show, if the pseudopotential approximation is valid. This potential is directly implemented in the MD method.

Thermal effects and cooling.

As it was mentioned previously, it is important to initialize the ions' temperature T . It is done directly, by placing ions with mass m with some initial velocity v , corresponding to the thermal distribution with a probability density function:

$$f(v) = \left(\frac{m}{2\pi k_B T} \right)^{\frac{3}{2}} e^{-\frac{mv^2}{2k_B T}}, \quad (4.6)$$

where k_B is a Boltzmann constant. The mean thermal velocity for the ion, produced in the oven (when the ions are distributed only in a half-space):

$$\langle v \rangle = \sqrt{\frac{\pi k_B T}{m}}. \quad (4.7)$$

The oven temperature is usually $T = 700$ K. However, along the path the ion passes to the trapping region, its velocity is typically reduced to that, corresponding to the $T \sim 50$. So the simulated ion loading occurs with this temperature^[26].

Then ions are cooled down to 0 K. In an experimental setup the laser cooling is implemented, which effectively applies the friction force $F_{cool} = -k\dot{r}$. This cooling can be simulated directly, but the more preferable way is to implement Langevin dynamics. Here, the friction force is similar to the laser cooling force F_{cool} . And the stochastic term represents the heating rate of the trap, which is extremely relevant to the SETs. This force also includes a non-ideal vacuum in the trap, although its influence is neglectful.

The stochastic force amplitude is also derived in terms of temperature. By applying a friction force the system's temperature is cooled down to 0, while the force applies random kicks to the ions. These random kicks eventually must increase the temperature of the system to the $T_{variable}$ over a long time. Choosing this temperature the heating is defined. In the case of planar traps, operational temperatures are measured in micro Kelvin, defined through the mean phonon number (see section 2.2.2). For the simulation it's appropriate to choose $T_{variable} = 0.01$ mK.

Normal modes in SET

In the diploma normal modes are calculated only for the linear ion chains according to section 2.3.2. Then, as the potential in the trapping region is considered harmonic, the normal modes are calculated by the (2.35-2.40), using only secular trap frequencies and its equilibrium positions, obtained through the crystallization of a Coulomb crystal.

4.2 SID package

For the MD simulation of ions in the surface electrode traps, the "Surface Ion Dynamics" (SID) Python package was implemented. It produces results according to 4.1.2. For the Coulomb interaction simulation and the cooling techniques a Python package LIon was used^[43]. The LIon package simulates ion dynamics in conventional 3D harmonic

Paul traps. The SID is an extension of this package, which uses the m2DIT package to simulate SET potential. Additionally it performs normal modes calculation.

The MD method is realized with LAMMPS software, which is a powerful tool for molecular dynamics with a wide range of functions. It allows potential scaling of the system and implementing MD simulations with highest precision. Also, the functionality of the software allows to conveniently implement additional functions, for future specifications.

4.2.1 Program description

The simulation starts after defining the planar trap by the m2DIT package. The results are obtained for the trap from section 4.5 – the trap designed for an ion computer with 5 ions (figure 4.2).

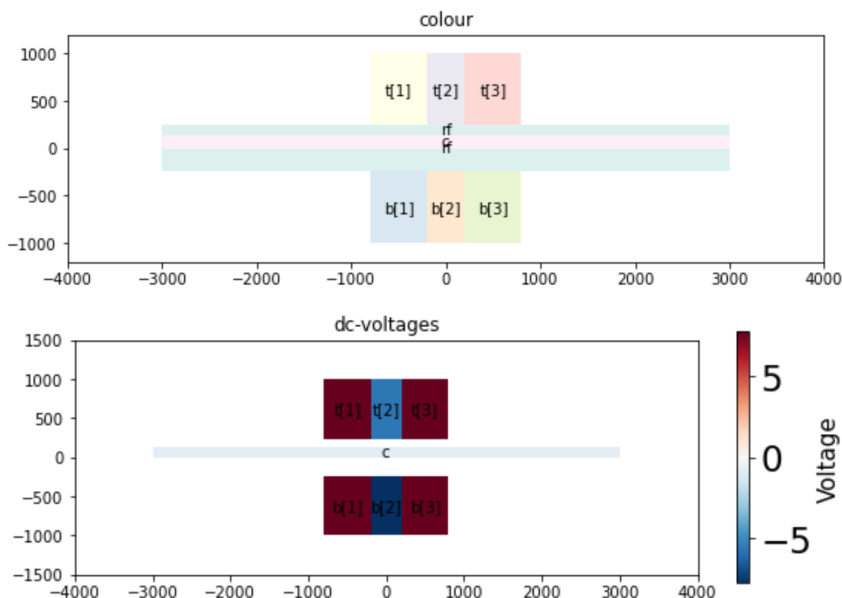


Figure 4.2: (upper) A simulated trap for the computer for 5 ions. The RF amplitude is 223 V, RF frequency $\Omega = 25.8$ MHz. (lower) The voltage set, applied to the electrodes.

The ions are specified in the respective *Ions()* class, which may contain different ion species, for example $^{40}\text{Ca}^+$ and $^{43}\text{Ca}^+$. The mixed species ion quantum computing is a wide area, which is out of scope of this diploma. All simulations are carried for $^{40}\text{Ca}^+$ ions.

Then the ions are placed with a *pylion.placeions()* pyLion package function, which makes a request to LAMMPS. It places the ions to the positions, passed as an argument of the function. The SID package creates several types of such positions by functions:

1. *min_ion_cloud()* – A random ion cloud around the potential minimum in the given radius.
2. *ion_in_order()* – Creates ions in the approximate minimum positions in the trap minimum.

Applying the *pylion.thermalvelocities()*, executing the respectful LAMMPS function, the initial velocities of the ions are defined, according to the thermal distribution. The temperature is set as 50 K.

Then, the trap is defined. The potential is applied separately from the Coulomb potential. The SID package allows to define several SETs:

1. *five_wire_trap()* – the simplest five wire trap, defined by the *FiveWireTrap()* function from the m2DIT package.
2. *ring_trap()* – the simplest point trap, which is represented by an array of ring RF electrodes, placed in a row. The point trap potential is not considered in this diploma, although was developed for the package.
3. *polygon_trap()* – a general polygon trap, which is defined as coordinates for DC and RF rectangular electrodes.
4. *point_trap()* – a general point trap, represented by an array of small circles with a respective voltage.
5. *square_trap()* – a special trap, designed as a proposal for trapped-ion quantum computer scaling. Its consideration is out of scope of this diploma.

After the trap is specified, a cooling is applied by the *pylion.langevinbath()*, which effectively implements Langevin dynamics for cooling. For an argument it passes the $T_{\text{variable}} = 0.01$ mK, and a damping time, defining the friction force $t_D = \gamma^{-1} = 10^{-7}$.

Then, the function *pylion.evolve()* is applied, executing the simulation via LAMMPS. The ions' coordinates are written to the file for each timestep, giving the trajectories for each ion.

For the researched trap, the ion crystal is depicted on the figure 4.3. This effectively indicates that ions are confined and stable in this trap, and condense into linear crystal phase. The final ion coordinates are demonstrated on table 4.1.

Table 4.1: Coordinates of the Coulomb crystal.

N	x	y	z
1	-6.98179e-06	9.99503e-05	0.000112142
2	-3.29319e-06	9.99549e-05	0.000112146
3	-5.34978e-20	9.99562e-05	0.000112147
4	3.29319e-06	9.99549e-05	0.000112146
5	6.98179e-06	9.99503e-05	0.000112142

On the figure 4.4 an ions' evolution along an axial axis is shown. It is clear that trajectories are initially oscillating from the thermal fluctuations, and then condense into unchanging Coulomb crystal.

After the positions of ions are obtained, the normal modes calculation is performed with functions *axial_normal_modes()* and *radial_normal_modes()*, which determine respective normal modes according to section 2.3.2. The resulting spectrum is shown on the figure 4.5 a). On the figure 4.5 b) an interaction matrix for 5 ions is depicted, according to (2.45).

The normal modes obtained for this trap for 5 ions are represented on the table 4.2. Calculated modes are verified in section 4.4.2. For the surface trap radial modes are different, since secular frequencies of y' and z' (rotated by the radial asymmetry of the trap), are different.

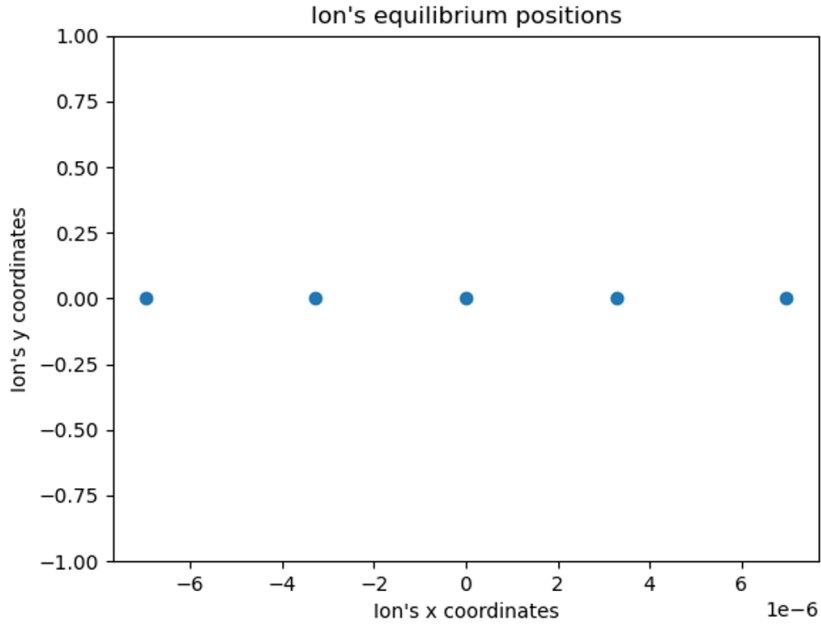


Figure 4.3: Positions of a linear ion chain, obtained for the manufactured trap. The distribution along z -axis is neglectful.

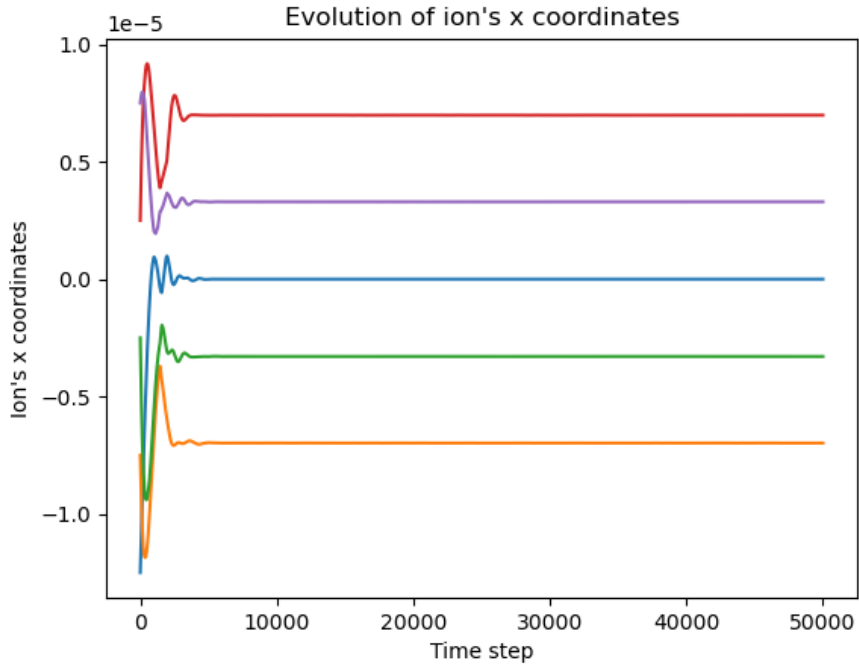


Figure 4.4: An ion positions' evolution along the z -axis. The timestep is chosen to be $1/(20\Omega)$.

4.2.2 Technical requirements

The SID package is an extension of the m2DIT package, so all the requirements from section 3.2.3 (along with the m2DIT package being installed itself) remain. Also the pyLion package must be installed. The 3Mar2020 build of LAMMPS software must be installed, although other versions of LAMMPS are appropriate with small modifications.

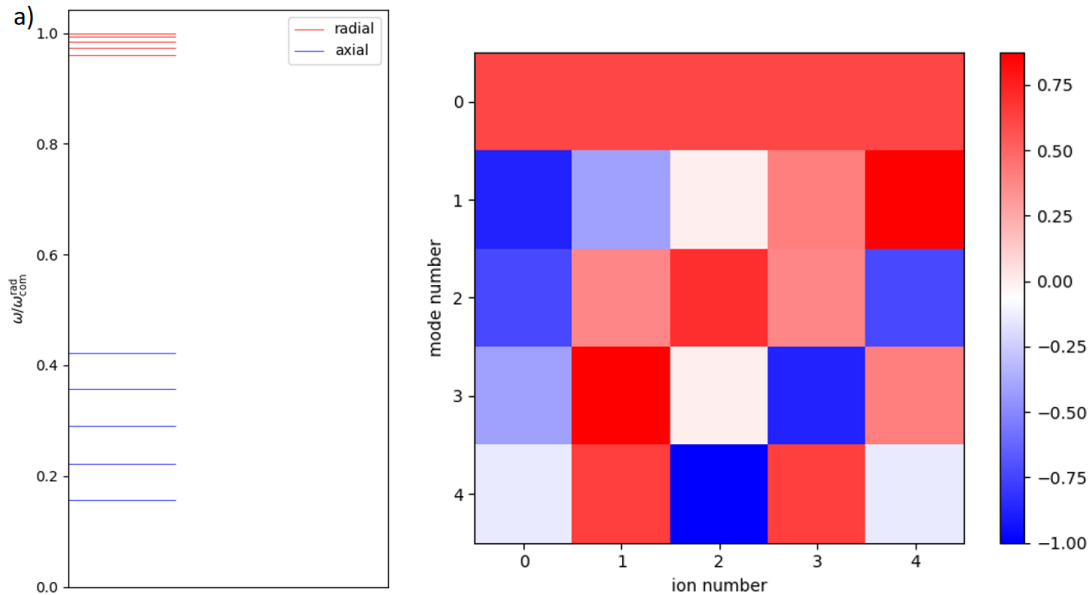


Figure 4.5: a) Normal modes' spectrum for 5 ions as a relation $\omega/\omega_{COM}^{rad}$. b) An interaction matrix for 5 ions. COM mode is the mode number 0. The color of the cell represents an interaction force of i^{th} ion with j^{th} mode.

Table 4.2: The normal modes for 5 ions. COM modes are highlighted blue.

	Mode frequency, MHz	Normalized mode vector
Axial x normal modes	1.17	[4.47e-01 4.47e-01 4.47e-01 4.47e-01 4.47e-01]
	2.02	[-6.39e-01 -3.02e-01 1.20e-04 3.02e-01 6.39e-01]
	2.82	[-5.37e-01 2.80e-01 5.14e-01 2.81e-01 -5.38e-01]
	3.57	[-3.02e-01 6.40e-01 -1.48e-04 -6.39e-01 3.01e-01]
	4.29	[1.05e-01 -4.70e-01 7.32e-01 -4.71e-01 1.05e-01]
Radial y' normal mode	6.86	[1.05e-01 -4.70e-01 7.32e-01 -4.71e-01 1.05e-01]
	7.06	[-3.02e-01 6.40e-01 -1.48e-04 -6.39e-01 3.01e-01]
	7.23	[-5.37e-01 2.80e-01 5.14e-01 2.81e-01 -5.38e-01]
	7.36	[-6.39e-01 -3.02e-01 1.20e-04 3.02e-01 6.39e-01]
	7.45	[4.47e-01 4.47e-01 4.47e-01 4.47e-01 4.47e-01]
Radial z' normal mode	6.96	[-1.05e-01 4.70e-01 -7.32e-01 4.71e-01 -1.05e-01]
	7.16	[3.02e-01 -6.40e-01 1.48e-04 6.39e-01 -3.01e-01]
	7.33	[-5.37e-01 2.80e-01 5.14e-01 2.81e-01 -5.38e-01]
	7.46	[-6.39e-01 -3.02e-01 1.20e-04 3.02e-01 6.39e-01]
	7.55	[4.47e-01 4.47e-01 4.47e-01 4.47e-01 4.47e-01]

Unlike the m2DIT package, SID is more demanding for the calculation power. It is possible to execute SID in the basic laptop, but the average simulation time for a simple trap is ~ 10 minutes. For a simulation with more complicated traps the high resourceful computer is required.

4.3 Phase transitions in Coulomb crystals

As mentioned in section 4.1.2, one of the simulation goals is to determine the phase of the Coulomb crystal. For quantum computing applications the linear ion chains are

most common. However, depending on the trap parameters, the phase of the crystal can change^[44]. On the figure 4.6 first four phases are shown in the 2D crystal.

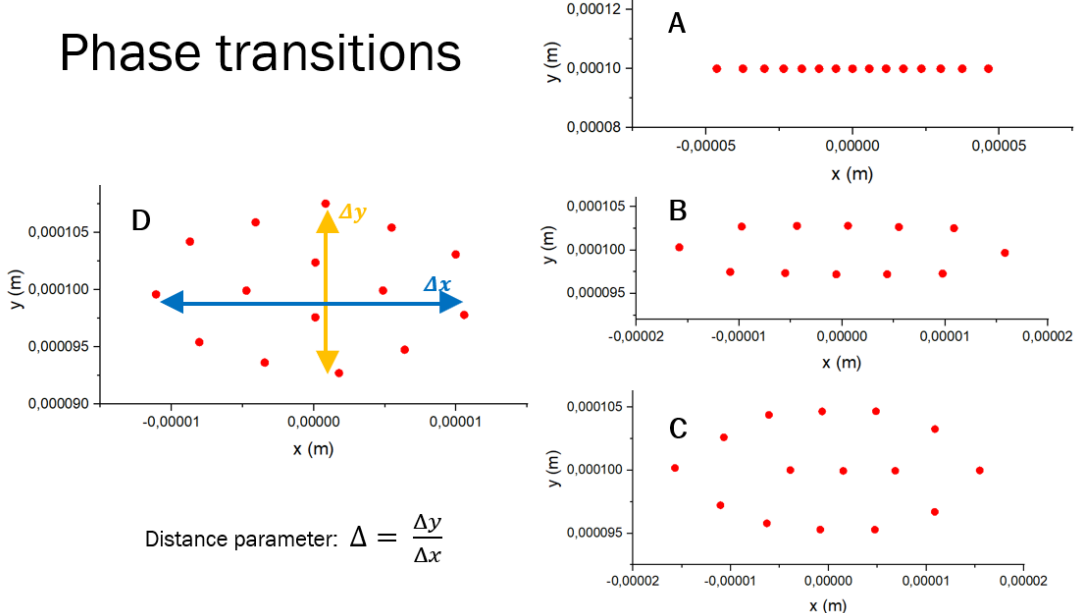


Figure 4.6: First four phases of 2D Coulomb crystals. A – linear phase, B – zigzag phase, C – ellipse, encircling a single ion, D – concentric ellipses. The distance parameter Δ serves as an indication of the phase transition. The results are obtained by direct simulation with SID of 12 and 15 ions.

The phase change depends on the anisotropy parameter α :

$$\alpha = \frac{\omega_{ax}^2}{\omega_{rad}^2}, \quad (4.8)$$

the relation of axial and radial secular frequency's squares. It can qualitatively be explained by the harmonic approximation. The secular frequency shows the curvature of the potential in the minimum. The more the frequency, the steeper the potential well. This potential well "squeezes" the ions, which are interacting as beads connected by springs, in the direction of the secular mode. Thus, if the radial squeezing is not strong enough, to compensate for axial squeezing, the ion will distribute along this radial axis.

Varying the voltage set, an anisotropy parameter is changing, which leads to the phase transitions eventually. Consider the 2D case, depicted on the figure 4.6. The only 2D distribution (in x - y plane) is achieved, by setting the voltages' set satisfying $\omega_z \gg \omega_x, \omega_y$. Then the distance parameter is introduced:

$$\Delta = \frac{\Delta y}{\Delta x}, \quad (4.9)$$

the relation of distances between the furthest ions along a given axis. This parameter demonstrates an abrupt rising, whenever the phase transitions occurs (see figure 4.7). These risings determine the critical anisotropy parameter for each phase transition. Doing this for different number of ions, one obtains a power law, which determines the critical anisotropy for linear-zigzag transition of the utmost importance^[44]:

$$\alpha_c = 2.53N^{-1.71}. \quad (4.10)$$

This relation allows to quickly determine the possibility of a nonlinear crystal for a given trap. These power laws are further discussed in the next section.

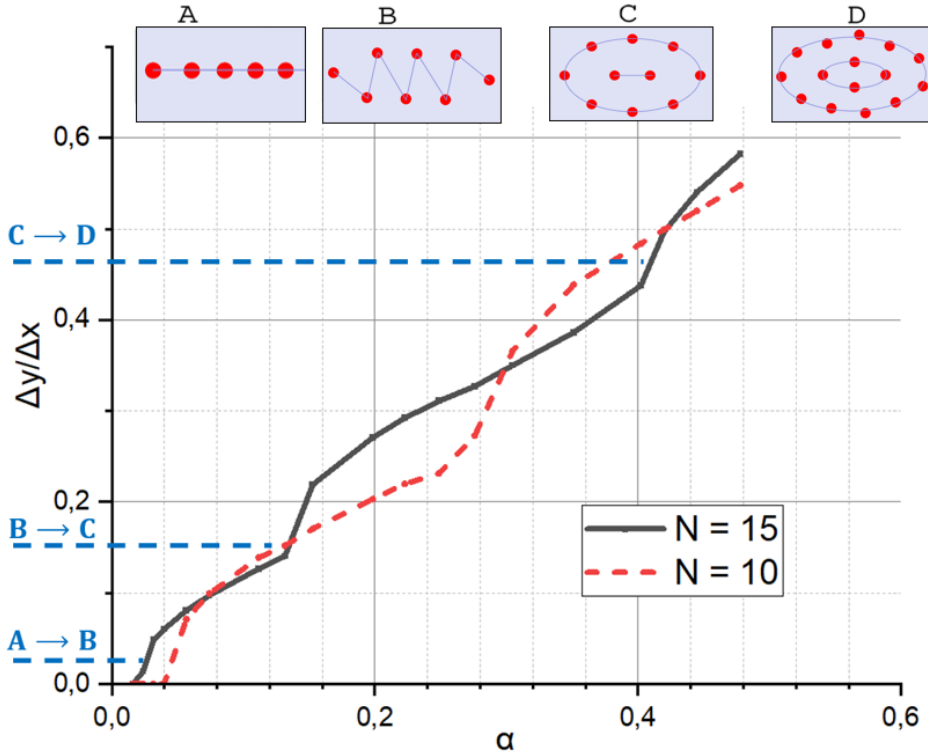


Figure 4.7: The plot of anisotropy α depending on distance parameter Δ . The abrupt rising of the graph indicates a phase transition. With that, the center of such rising is taken for a critical anisotropy α_c . The plots are obtained for 10 and 15 ions, simulated with SID by varying a voltage set.

4.4 Verification

4.4.1 Ion crystal

The verification protocol relies on the results from [44]. In this nature article, an experimental research to obtain power laws for phase transitions was carried out. The simulation ability is tested on their experimental results.

On the figure 4.8 a) a trap layout from the article is shown. Varying the voltages of ME electrodes, an anisotropy α was changed. AE electrode then compensated the potential minimum displacement. This layout was specifically designed for the trapping of many ions in the wide harmonic region. The size scale is ~ 10 mm, and the RF amplitude $U = 640$ V, RF frequency $\Omega = 15.37$ MHz, thus obtaining a giant trap depth of ~ 2 eV. The same trap for SID simulations is demonstrated on the figure 4.8 b).

The article provided an ion crystal form for several anisotropy parameters, and for the verification a simulation of 10 ions in the trap with $\alpha = 0.027$ was carried out. The figure 4.9 shows the results of an experiment (a), and SID simulation (b), which are practically the same.

Due to the lack of exact coordinates from [44], the length of a full ion chain, and the mean ion separation were calculated, and represented on the table 4.3. These results evaluate the SID accuracy by 98%.

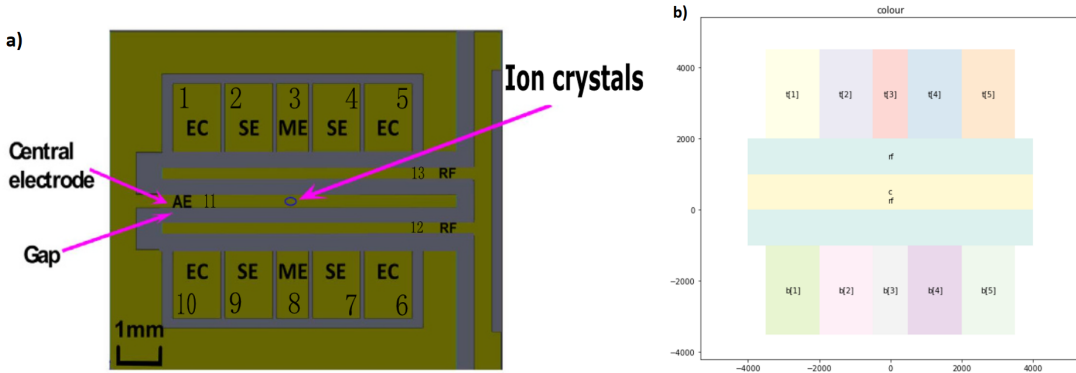


Figure 4.8: a) A trap layout from [44]. ME electrodes were used for tuning α . b) The similar trap, programmed by SID. Here the gapless approximation dictates us to fill the gaps between the electrodes by their equal extension^{House}.

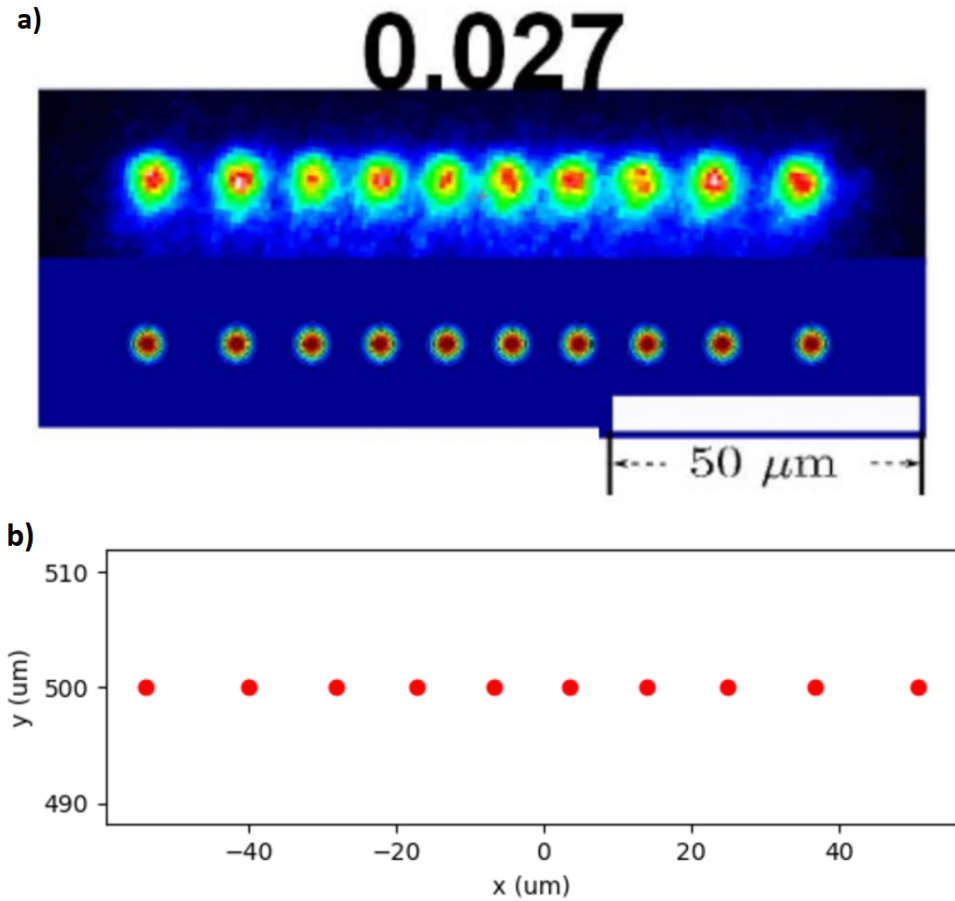


Figure 4.9: a) An experimental picture (upper) and the numerical calculation (lower) of the ion positions for $\alpha = 0.027$ in the [44]. b) The SID simulation with the same parameters. The results are practically the same.

4.4.2 Transition law

The results on table 4.3 represent a special case of linear crystals. To research a more general ion motion, it was decided to repeat the power law from (4.10). The trap layout was chosen differently from the one from figure 4.8, to prove a general character of the

Table 4.3: Comparison with [44]

	Ion chain length	Mean separation
Result in [44]	106.6 μm	11.8 μm
Result from SID	104.9 μm	11.7 μm

power law. The trap for the research is pictured on figure 4.10.

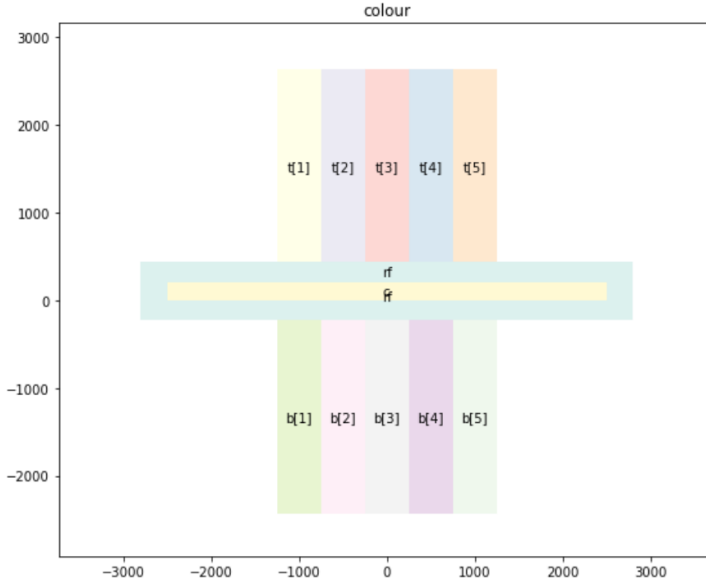


Figure 4.10: The trap, used for power law derivation. The trap scale is roughly half of the trap from [44]. The secular frequencies in the radial plane are $\omega_y \sim 3.4$ MHz, and $\omega_z \sim 4.2$, which is enough to ensure 2D crystal distribution in the x - y plane. RF amplitude is 216 V, and frequency $\Omega = 21$ MHz. Varying the electrodes with index 3, an anisotropy α is varied. Central electrode "c", depicted yellow, is used for micromotion compensation.

The trap is two times smaller, then the trap from [44], and RF lines are much thinner, which makes the harmonic region of the potential narrower. Then, varying anisotropy α , the plot of $\Delta(\alpha)$ was obtained. On the figure 4.7 the plots for 10 and 15 ions are shown. Additionally, 8 and 12 ions were measured.

The results for the power laws for critical anisotropy for two first phase transitions are demonstrated on the figure 4.11. The power laws are represented on table 4.4. The A-B transition is matching with good accuracy, but the B-C transition is different, with only the character of the law preserved. This fact is explained not only by the finite accuracy of the SID simulation, but with the fundamental differences between two researched traps.

Table 4.4: The power laws for critical anisotropy: $\alpha_{c_i} = C_i e^{\beta_i}$.

Parameters	Our simulation	Previous experiments
C_1	2.65 ± 0.48	2.53 ± 0.45
β_1	-1.75 ± 0.08	-1.71 ± 0.08
C_2	15.2 ± 2.1	8.65 ± 1.35
β_2	-1.71 ± 0.11	-1.47 ± 0.07

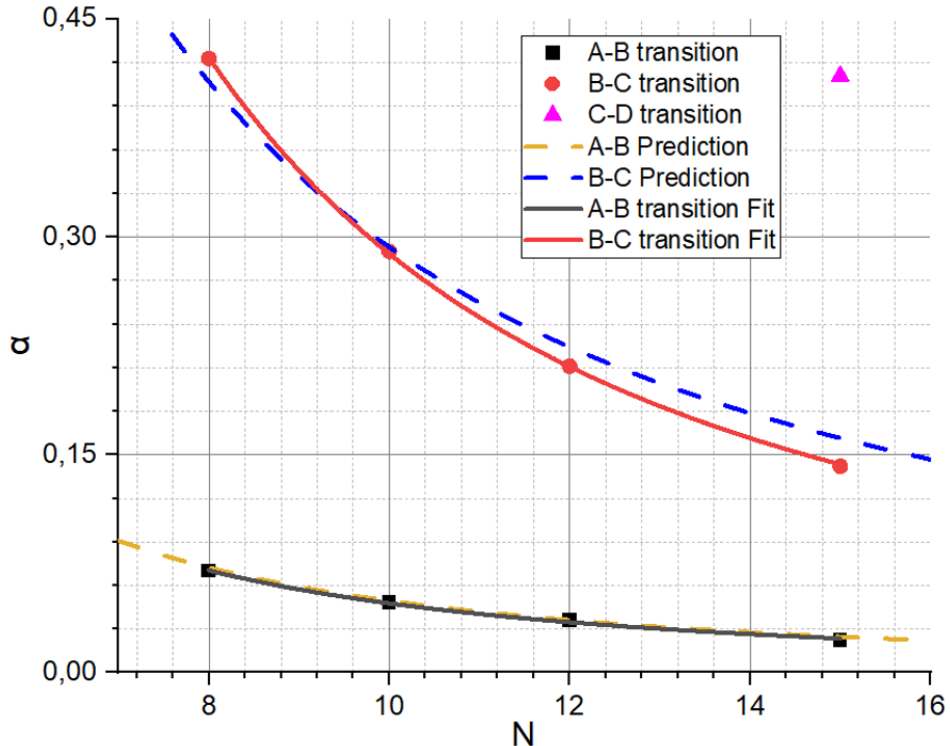


Figure 4.11: The plots of the power laws for first and second phase transitions. The dashed lines are the experimental results from [44], and solid lines are the power laws, obtained with the SID. While the first transition (linear to zigzag) matches perfectly, the second transition (zigzag to ellipse) doesn't fit well. This can be understood as an influence of anharmonic potential from different trap.

The main result of the [44] was an experimental demonstration of the second phase transition zigzag-ellipse. This transition occurs in the y direction, being distributed from the minimum axis further. However, in the trap from [44], the big scale of the trap employs a harmonic potential in the wide $x-y$ region. However, the narrower region in the researched trap, employs an influence of the anharmonicities^[45]. So, the wider distribution in the y direction makes ions subject to anharmonic potential, which changes the power law for this transition. This influence of the anharmonicity is a topic for the following research.

4.4.3 Normal modes verification

The verification of normal modes calculation can be carried out by the comparison of the obtained axial modes on the table 4.2 with the direct calculation on the figure 2.9. According to (2.39), the axial frequencies for 5 ions are calculated. Using $\omega_x = 1.168$ MHz, the calculated axial frequencies are demonstrated on the table 4.5. For the mode vectors' verification, the quadratic difference between vectors was calculated: $\sqrt{|\mathbf{u}_{\text{numerical}} - \mathbf{u}_{\text{theory}}|^2}$. Then, theoretical frequencies are denoted as ν_{theory} , numerically evaluated by SID: $\nu_{\text{numerical}}$. The table shows a good accuracy of the model.

Table 4.5: Comparison of Axial normal modes, calculated theoretically and numerically.

ν_{theory} , MHz	$ \nu_{\text{theory}} - \nu_{\text{numerical}} $, MHz	$\sqrt{ \mathbf{u}_{\text{numerical}} - \mathbf{u}_{\text{theory}} ^2}$
1.17	0	3.04×10^{-5}
2.02	2.17×10^{-3}	2.94×10^{-4}
2.82	4.14×10^{-3}	6.66×10^{-4}
3.57	5.35×10^{-3}	8.91×10^{-4}
4.29	6.57×10^{-3}	7.52×10^{-4}

4.5 Result: trap design for five ions

As a result of the work, a planar trap for 5 ions was designed. The gds-file is pictured on the figure 4.12 a). The previous simulations from section 4.2 were carried for this trap. The gds-file is passed to the manufacturing process, which is implemented by microfabrication in the clean room. The traps are usually fabricated on the chips, containing ~ 50 traps (figure 4.12 b)). The traps are then separated by simple cutting.

The parameters of ion traps, obtained by the simulation, are presented on the table 4.6.

Table 4.6: Parameters of the trap for 5 ions.

Parameter	Value
Trap depth	0.897 eV
ω_x	1.169 MHz in direction [1, 0, 0]
ω_y	7.779 MHz in direction [0, 0.98, -0.2]
ω_z	8.694 MHz in direction [0, 0.2, 0.98]
Potential minimum	[0, 100, 114] μm
Ion positions	See table 4.1
Normal modes	See table 4.2

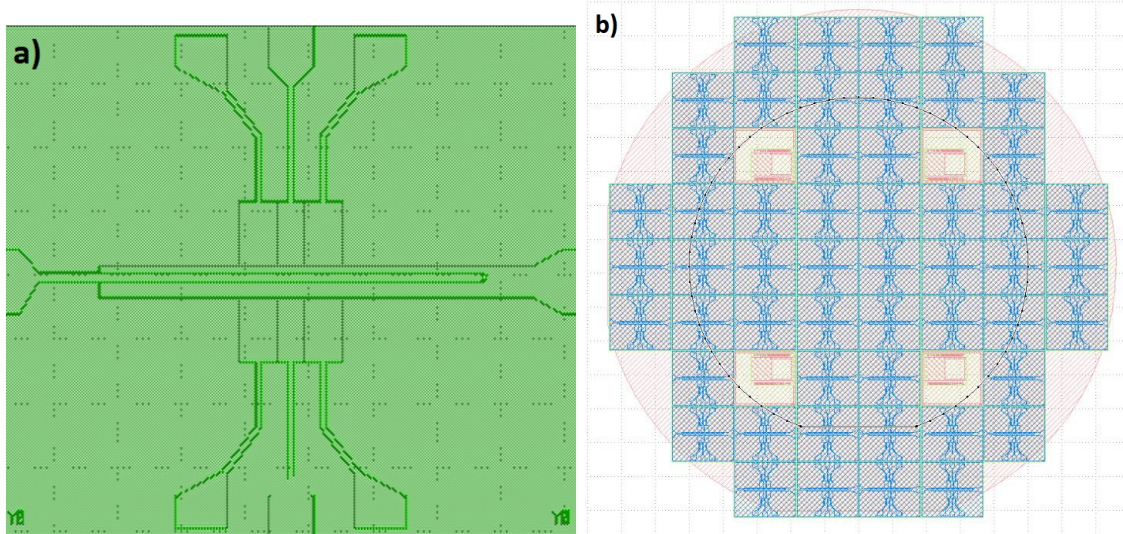


Figure 4.12: a) A trap layout for experimental manufacturing. The electrodes' voltages are passed through the wires, contacting the rest scheme. b) The chip microfabrication process. The chip contains roughly 50 traps, which are later separated for an experimental setup.

The figure 4.12 a) shows the wires supplying the voltages to electrodes. The trap is only a part of the complicated experimental setup, containing vacuum chamber, cryostat, and complicated electrical and optical systems for ion control. The diploma covers only a small part of the trapped-ion quantum computing.

Chapter 5

Conclusion

5.1 Summary

In the diploma, the theory of the ion-trapping in Surface Electrode Traps is discussed. The package m2DIT for modeling of the potential above the trap's surface and calculating the trap parameters is presented. The package is in the process of registration as a patent for the Russian Quantum Center. The package SID for simulation of ion motion in the SETs and calculation of normal modes is presented. This package is also in the process of patent registration.

Using these packages, a design for the trap for 5 ions was derived. The parameters describing the trap were calculated. The trap was microfabricated, and is presented on the picture 5.1.

5.2 Comparison with existing results

5.2.1 SET simulation

There are several approaches to trapped-ion simulation. The main advantages of the m2DIT package are its speed and convenience. This allows a fast varying of trap parameters to determine the most optimal ones.

The package electrode-master on Python is a source of functions that calculate the potential distributions for surface traps. But it requires an additional code for those functions to be used. And the m2DIT package effectively provides such a practical tool.

The Python electrode-master package is based on the Mathematica package Surface Pattern^[29], which effectively provides the same functions. But the Python environment is more flexible for additional development.

The most accurate method for simulating the potential field is to use COMSOL software, which provides a wide range of electromagnetic simulations. However, it doesn't provide such convenience in the research process, so the Python package is more preferable for initial design. For the most accurate analysis the trap, developed by the m2DIT package, should be simulated in COMSOL before manufacture.

5.2.2 Ion dynamics simulation

For ion dynamics simulation in surface traps there is no uniform software. For the practical needs scientific groups are usually carrying a custom MD simulation, or just potential minimization to obtain ions' equilibrium positions. The advantage of the SID package

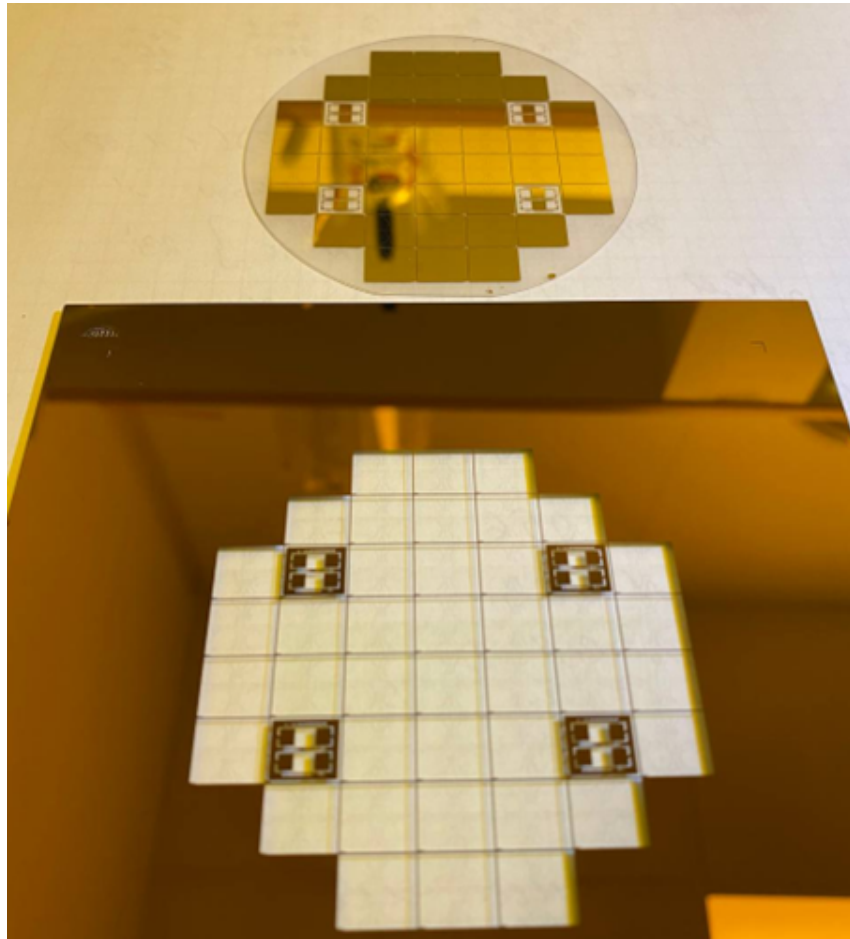


Figure 5.1: A microfabricated trap for 5 ions. The golden plate chip contains 40 traps, and 4 complicated electrode structures, which are implemented to experimentally determine the abilities of the manufacturing.

is its high efficiency due to LAMMPS integration, and a general approach to choose an arbitrary trap.

The ion dynamics can also be simulated in COMSOL, however it requires enormous computational power, and therefore also is not convenient for the research. The most efficient way is also developing the trap with Python SID package, and then running the COMSOL simulation before microfabrication.

5.3 Outlook

The packages will continue to be used for the fast simulations and derivation of the traps in the future. There are several projects, based on this research, that will be developed further.

First of all, a brand new SET design was developed as a scaling proposal for an ion computer. This study is in the process of the research, and the following scientific paper is expected to be published in the Q1 journal.

The diploma study reveals the requirement of a stability theory for several ions in the trap, which is a direction of a future research, using the SID package, which shows if the motion is truly stable.

Finally, the simulation of phase transitions demonstrates the anharmonicity influence

on the transitions' law. The research developing the model of such dependence will be carried out.

The group direction for surface trap research is pointed towards complication of the traps. Multilayered traps^[46] and traps with integrated SNSPD detectors and photonic waveguides^[47] are being developed. All these traps can't be efficiently simulated with the SID package or its improvements, and the COMSOL simulations for such traps are necessary. The Python packages will still be used for an initial research, and understanding of principle behavior of the system, but for the more accurate simulations COMSOL will be used.

Bibliography

- [1] *Nielsen, M.* Introduction and overview / M. Nielsen, I. Chuang // Quantum computation and Quantum Information / Ed. by M. Nielsen, I. Chuang, Simon Capelin, Margaret Patterson. — Cambridge University Press, 2010.
- [2] *McGeoch, Catherine C.* Quantum Annealing / Catherine C. McGeoch // Adiabatic Quantum Computation and Quantum Annealing / Ed. by Lanzagorta M., Uhlmann J. — Morgan Claypool Publishers, 2014.
- [3] *McGeoch, Catherine C.* Adiabatic Quantum Computation / Catherine C. McGeoch // Adiabatic Quantum Computation and Quantum Annealing / Ed. by Lanzagorta M., Uhlmann J. — Morgan Claypool Publishers, 2014.
- [4] *R., Raussendorf.* A One-Way Quantum Computer / Raussendorf R., Briegel H. // *Phys. Rev. Lett.* — 2001. — Vol. 86.
- [5] Noisy intermediate-scale quantum algorithms / Kishor Bharti, Alba Cervera-Lierta, Thi Ha Kyaw et al. // *Rev. Mod. Phys.* — 2022. — Vol. 94.
- [6] *Shor, Peter W.* Polynomial-Time Algorithms for Prime Factorization and Discrete Logarithms on a Quantum Computer / Peter W. Shor // *SIAM Journal on Computing*. — 1997. — Vol. 26.
- [7] Quantum computing at the quantum advantage threshold: a down-to-business review / A.K. Fedorov, N. Gisin, S.M. Belousov, A.I. Lvovsky. — arXiv:2203.17181 [quant-ph].
- [8] *Knill, E.* Quantum computing with realistically noisy devices / E. Knill // *Nature*. — 2005. — Vol. 434.
- [9] *Cirac, J. I.* Quantum Computations with Cold Trapped Ions / J. I. Cirac, P. Zoller // *Phys. Rev. Lett.* — 1995. — Vol. 74.
- [10] Trapped-ion quantum computing: Progress and challenges / Colin D. Bruzewicza, John Chiaverinib, Robert McConnellc, Jeremy M. Saged // *Applied Physics Reviews*. — 2019. — Vol. 6.
- [11] *DiVincenzo, David P.* The Physical Implementation of Quantum Computation / David P. DiVincenzo // *Progress of Physics*. — 2000. — Vol. 48.
- [12] *Pino, J.M.* Demonstration of the trapped-ion quantum CCD computer architecture / J.M. Pino, J.M. Dreiling, C. et al Figgatt // *Nature*. — 2021. — Vol. 592.
- [13] *Chiaverini, J.* Surface-electrode architecture for quantum information processing / J. Chiaverini, et al // *Quantum information and computation*. — 2005. — Vol. 5.

- [14] Chip-Integrated Voltage Sources for Control of Trapped Ions / J. Stuart, R. Panock, C.D. Bruzewicz et al. // *Phys. Rev. Applied.* — 2019. — Vol. 11.
- [15] Shuttling-based trapped-ion quantum information processing / V. Kaushal, B. Lekitsch, A. Stahl et al. // *AVS Quantum Sci.* — 2020. — Vol. 2.
- [16] *Paul, Wolfgang.* Electromagnetic traps for charged and neutral particles / Wolfgang Paul // *Rev. Mod. Phys.* — 1990. — Vol. 62.
- [17] *Niedermayr, Michael.* Cryogenic surface ion traps: Ph.D. thesis / Fakultät für Mathematik, Informatik und Physik der Leopold-Franzens-Universität Innsbruck. — 2015.
- [18] Design of blade-shaped-electrode linear ion traps with reduced anharmonic contributions / K. Deng, H. Che, Y. Lan et al. // *J. Appl. Phys.* — 2015. — Vol. 118.
- [19] *Shaertl, Dominic.* — High temperature superconducting ion traps. — Master thesis, Leopold-Franzens University of Innsbruck, 2016.
- [20] Ground-State Cooling of a Single Atom at the Center of an Optical Cavity / Andreas Reiserer, Christian Nölleke, Stephan Ritter, Gerhard Rempe // *Phys. Rev. Lett.* — 2013. — Vol. 110.
- [21] Electromagnetically-induced-transparency ground-state cooling of long ion strings / Regina Lechner, Christine Maier, Cornelius Hempel et al. // *Phys. Rev. A.* — 2016. — Vol. 93.
- [22] *Heinrich, Johannes M.* A Be⁺ Ion Trap for H₂⁺ Spectroscopy: Ph.D. thesis / SORBONNE UNIVERSITÉ. — 2015.
- [23] *Holzman, Itamar.* Superconducting Nanowires for Single-Photon Detection: Progress, Challenges, and Opportunities / Itamar Holzman, Yachin Ivry // *Advanced Quantum Technologies.* — 2019. — Vol. 2.
- [24] *James, D.F.V.* Quantum dynamics of cold trapped ions with application to quantum computation / D.F.V. James // *Appl. Phys. B.* — 1998. — Vol. 66.
- [25] *Sosnova, K.* Character of motional modes for entanglement and sympathetic cooling of mixed-species trapped-ion chains / K. Sosnova, A. Carter, C. Monroe // *Phys. Rev. A.* — 2021. — Vol. 103.
- [26] *Malinowski, Maciej.* Unitary and Dissipative Trapped-Ion Entanglement Using Integrated Optics: Ph.D. thesis / ETH Zurich. — 2021.
- [27] *House, M. G.* Analytic model for electrostatic fields in surface-electrode ion traps / M. G. House // *Phys. Rev. A.* — 2008. — Vol. 78.
- [28] *Cesari, Lamberto.* Nonlinear systems / Lamberto Cesari // Asymptotic Behavior and Stability Problems in Ordinary Differential Equations. — Springer Berlin, Heidelberg, 1971.
- [29] *Schmied, Roman.* Optimal Surface-Electrode Trap Lattices for Quantum Simulation with Trapped Ions / Roman Schmied, Janus H. Wesenberg, Dietrich Leibfried // *Phys. Rev. Lett.* — 2009. — Vol. 102.

- [30] *Schmied, Roman.* Electrostatics of gapped and finite surface electrodes / Roman Schmied // *New J. Phys.* — 2010. — Vol. 12.
- [31] Experimental investigation of planar ion traps / C. E. Pearson, D. R. Leibrandt, W. S. Bakr et al. // *Phys. Rev. A.* — 2006. — Vol. 73.
- [32] *Schmied, Roman.* Quantum simulation of the hexagonal Kitaev model with trapped ions / Roman Schmied, Janus H. Wesenberg, Dietrich Leibfried // *New J. Phys.* — 2011. — Vol. 13.
- [33] *Shaikh, Fayaz A.* Stability analysis of ion motion in asymmetric planar ion traps / Fayaz A. Shaikh, Arkadas Ozakin // *J. Appl. Phys.* — 2012. — Vol. 112.
- [34] *Jördens, R.* Numerical tools for rf ion traps. — 2016. — <https://github.com/nist-ionstorage/electrode>.
- [35] Comparison of methods for finding saddle points without knowledge of the final states / R. A. Olsen, G. J. Kroes, G. Henkelman, et al // *J. Chem. Phys.* — 2004. — Vol. 121.
- [36] Observation of superconductivity and surface noise using a single trapped ion as a field probe / K. Lakhmanskii, P. C. Holz, D. Schärtl et al. // *Phys. Rev. A.* — 2019. — Vol. 99.
- [37] COMSOL documentation, 2022. — <https://doc.comsol.com/6.0/docserver/#!com.comsol.help.comsol/helpdesk/helpdesk.html>.
- [38] Molecular dynamics simulations: advances and applications / Adam Hospital, Josep Ramon Goñi, Modesto Orozco, Josep L Gelpí // *Advances and Applications in Bioinformatics and Chemistry.* — 2015. — Vol. 2015:8.
- [39] *Adcock, Stewart A.* Molecular Dynamics: Survey of Methods for Simulating the Activity of Proteins / Stewart A. Adcock, J. Andrew McCammon // *Chem. Rev.* — 2006. — Vol. 106.
- [40] LAMMPS documentation, 2022. — <https://doc.lammps.org>.
- [41] A computer simulation method for the calculation of equilibrium constants for the formation of physical clusters of molecules: Application to small water clusters / William C. Swope, Hans C. Andersen, Peter H. Berens, et al // *J. Chem. Phys.* — 1982. — Vol. 76.
- [42] Structural and energetic properties of molecular Coulomb crystals in a surface-electrode ion trap / William C. Swope, Hans C. Andersen, Peter H. Berens, et al // *New J. Phys.* — 2015. — Vol. 17.
- [43] *E.Bentine. (py)LLion*: A package for simulating trapped ion trajectories / E.Bentine, C.J.Foota, D.Trypogeorgos // *Computer Physics Communications.* — 2020. — Vol. 253.
- [44] Exploring structural phase transitions of ion crystals / L. L. Yan, W. Wan, L. Chen et al. // *Scientific Reports.* — 2016. — Vol. 6.
- [45] Normal modes of trapped ions in the presence of anharmonic trap potentials / J P Home, D Hanneke, J D Jost et al. // *New J. Phys.* — 2011. — Vol. 13.

- [46] Multilayer ion trap technology for scalable quantum computing and quantum simulation / A Bautista-Salvador, G Zarantonello, H Hahn et al. // *New J. Phys.* — 2019. — Vol. 21.
- [47] *Kim, Tony Hyun.* Surface-electrode ion trap with integrated light source / Tony Hyun Kim, Peter F. Herskind, Isaac L. Chuang // *Appl. Phys. Lett.* — 2011. — Vol. 98.